Ultrasonics - Sonochemistry 61 (2020) 104839

Contents lists available at ScienceDirect

Ultrasonics - Sonochemistry

journal homepage: www.elsevier.com/locate/ultson

Impact of sonochemical synthesis condition on the structural and physical properties of $MnFe_2O_4$ spinel ferrite nanoparticles

Raghvendra Singh Yadav[a,*], Ivo Kuřitka[a], Jarmila Vilcakova[a], Thaiskang Jamatia[a], Michal Machovsky[a], David Skoda[a], Pavel Urbánek[a], Milan Masař[a], Michal Urbánek[a], Lukas Kalina[b], Jaromir Havlica[b]

[a] Centre of Polymer Systems, University Institute, Tomas Bata University in Zlín, Trida Tomase Bati 5678, 760 01 Zlín, Czech Republic
[b] Materials Research Centre, Brno University of Technology, Purkyňova 464/118, 61200 Brno, Czech Republic

ARTICLE INFO

Keywords:
Spinel ferrite
Nanoparticles
Sonochemical synthesis
Magnetic property
Electrical property

ABSTRACT

Herein, we report sonochemical synthesis of $MnFe_2O_4$ spinel ferrite nanoparticles using UZ SONOPULS HD 2070 Ultrasonic homogenizer (frequency: 20 kHz and power: 70 W). The sonication time and percentage amplitude of ultrasonic power input cause appreciable changes in the structural, cation distribution and physical properties of $MnFe_2O_4$ nanoparticles. The average crystallite size of synthesized $MnFe_2O_4$ nanoparticles was increased with increase of sonication time and percentage amplitude of ultrasonic power input. The occupational formula by X-ray photoelectron spectroscopy for prepared spinel ferrite nanoparticles was $(Mn_{0.29}Fe_{0.42})[Mn_{0.71}Fe_{1.58}]O_4$ and $(Mn_{0.28}Fe_{0.54})$ $[Mn_{0.72}Fe_{1.46}]O_4$ at sonication time 20 min and 80 min, respectively. The value of the saturation magnetization was increased from 1.9 emu/g to 52.5 emu/g with increase of sonication time 20 min to 80 min at constant 50% amplitude of ultrasonic power input, whereas, it was increased from 30.2 emu/g to 59.4 emu/g with increase of the percentage amplitude of ultrasonic power input at constant sonication time 60 min. The highest value of dielectric constant (ε′) was 499 at 1 kHz for nanoparticles at sonication time 20 min, whereas, ac conductivity was 368×10^{-9} S/cm at 1 kHz for spinel ferrite nanoparticles at sonication time 20 min. The demonstrated controllable physical characteristics over sonication time and percentage amplitude of ultrasonic power input are a key step to design spinel ferrite material of desired properties for specific application. The investigation of microwave operating frequency suggest that these prepared spinel ferrite nanoparticles are potential candidate for fabrication of devices at high frequency applications.

1. Introduction

Recently, nanoparticles of spinel ferrite have received a considerable attention among researchers due to its widespread technological applications such as magnetic resonance imaging (MRI) contrast agent, drug-delivery, magnetically recoverable efficient photo-catalyst, ferrofluids, gas sensor, hyperthermia cancer treatment, magnetic refrigeration (MR), anode material for Li-ion battery, magnetic recording media with higher storage density, microwave devices, spintronic devices, super-capacitors, paint industry, and water splitting for hydrogen production, etc. [1–5]. In addition, the magnetic and dielectric characteristics of spinel ferrite nanoparticles make them very attractive functional material. In spinel ferrite with general formula AFe_2O_4 (A = Mn^{2+}, Ni^{2+}, Co^{2+}, etc.), there is a cubic close-packed oxygen lattice with metal ions inhabiting 1/8 of the tetrahedral and 1/2 of the octahedral voids. Therefore, the number of tetrahedrally coordinated ionic types in the system (8 per unit cell) is half of the octahedrally coordinated (16 per unit cell). The system in which A^{2+} and Fe^{3+} ions fully sited on the tetrahedral and octahedral site, respectively, is normal spinel system, whereas, the A^{2+} ions occupied the octahedral sites with half of the Fe^{3+} ions located on tetrahedral sites is inverse spinel. In partial spinel structure, a fraction of A^{2+} ions, known as inversion degree, located on the octahedral site. In the bulk, $MnFe_2O_4$ is partially inverse, $NiFe_2O_4$ and $CoFe_2O_4$ are inverse, and $ZnFe_2O_4$ is a normal spinel [6]. However, the spinel ferrite nanoparticles exhibit high level of cation inversion [7]. B. Nandan et al. [8] reported the cation inversion in Co^{2+} doped $NiFe_2O_4$ nanoparticles. M. Fantauzzi et al. [9] noticed the cation inversion in $CoFe_2O_4$ spinel ferrite nanoparticles. S. K. Gore et al. [10] observed the cation inversion in Bi^{3+} doped $CoFe_2O_4$ nanoparticles.

For technological applications, the performance of spinel ferrite can be regulated by particle size, microstructure, cation distribution at

* Corresponding author.
E-mail address: yadav@utb.cz (R. Singh Yadav).

https://doi.org/10.1016/j.ultsonch.2019.104839
Received 14 August 2019; Received in revised form 18 October 2019; Accepted 21 October 2019
Available online 23 October 2019
1350-4177/

octahedral and tetrahedral sites, etc [11]. A research group, E. Ranjith Kumar et al. [12] investigated particle size dependent physical properties of spinel ferrite nanoparticles. Another research group, L. Zhang et al. [13] noticed the dependence of physical characteristics on the microstructure of spinel ferrite nanoparticles. M. Abbas et al. [14] observed the size-controlled physical properties of cobalt ferrite nanostructures. Further, L. I. Granone et al. [15] noticed the influence of degree of inversion in $ZnFe_2O_4$ spinel ferrite on the electrical conductivity. V. G. Harrisa et al. [16] reported the effect of cation inversion in spinel ferrite nanoparticles on the physical properties. R. Lamouri, et al. [17] investigated the impact of cation inversion on the magnetic properties of spinel ferrite. Furthermore, L. I. Granone et al. [18] reported the impact of the degree of inversion in spinel ferrite on optical characteristics. In addition, L. I. Granone et al. [19] observed the influence of the cation redistribution on the photoelectrochemical activity.

A controllable nucleation and growth of nanoparticles during chemical synthesis can provide desired physical properties for specific application. Spinel ferrite nanoparticles have been synthesized by several chemical synthesis approach such as hydrothermal method, co-precipitation method, microemulsion method, sol-gel method, sonochemical method, solution combustion method, etc. [20,21]. A research group, P. Dolcet et al. [7] noticed the various level of inversion in spinel ferrite nanoparticles by wet chemical synthesis. In addition, S.I. El-Dek et al. [22] observed the influence of different chemical synthesis method on the physical properties of spinel ferrite. Among chemical synthesis approaches, the sonochemical synthesis method is one of the chemical synthesis approach for the preparation of spinel ferrite nanoparticles with controllable particle size, morphology and its physical characteristics [23,24]. In sonochemical synthesis method, the chemical impact of ultrasonic irradiation arises from acoustic cavitation, i.e., the rapid formation, growth and implosive collapse of consecutive generated bubbles in liquid medium [25,26]. Further, the collapse of bubble provides the creation of an instantaneously high thermal energy and pressure pulse within a very few time. These conditions provide formation of noble nanostructures [27,28]. The significant advantage of this sonochemical synthesis approach is the cost-effectiveness, high reaction rate, controllable synthesis condition, high purity, narrow size distribution, environmentally friendly nature and scalability, etc. [29,30]. These advantages make this synthesis technique as potential alternative than other chemical synthesis approaches [31,32].

In our previous report, we investigated the impact of Gd^{3+} substitution in $CoFe_2O_4$ nanoparticles synthesized by sonochemical method on its physical properties [33]. Other research group, P. Balasubramanian et al. [34] reported the sonochemical synthesis of calcium ferrite and its application as electrochemical sensor. Further, N. Lenin et al. [35] observed the impact of neodymium ion in $NiFe_2O_4$ spinel ferrite nanoparticles prepared by sonochemical method on its structural, dielectric and magnetic properties. Furthermore, S. R. Yousefi et al. [36] investigated the impact of sonication time and power in sonochemical preparation of $ZnFe_2O_4$ nanostructures and further studied its photocatalytic activity. In addition, M.A. Almessiere et al. [37,38] reported the impact of Gd^{3+} and Tm^{3+} ion in cobalt ferrite nanoparticles synthesized by sonochemical method on its structural, optical and magnetic properties.

In the present work, we report the preparation of $MnFe_2O_4$ spinel ferrite nanoparticles by sonochemical synthesis approach via. controllable sonochemical synthesis time and percentage amplitude of ultrasonic power input. The structural evolution of $MnFe_2O_4$ nanoparticles over sonochemical synthesis conditions have been investigated in details. In addition, physical characteristics such as magnetic, optical, dielectric, electrical, impedance, modulus spectroscopy, and operating microwave frequency characteristics have been investigated in-depth.

2. Experimental section

2.1. Materials

The reagents Iron Nitrate [$Fe(NO_3)_3{\cdot}9H_2O$], Manganese nitrate [$Mn(NO_3)_2{\cdot}4H_2O$,] and sodium hydroxide (NaOH) were purchased from Alfa Aesar GmbH & Co KG, Germany.

2.2. Preparation

In the sonochemical synthesis of $MnFe_2O_4$ spinel ferrite nanoparticles, the sonication time was varied as 20 min, 40 min, 60 min and 80 min. For preparation, 2.6 g of $Mn(NO_3)_2{\cdot}4H_2O$ and 7.54 g of $Fe(NO_3)_2{\cdot}9H_2O$ was added in a beaker containing 60 ml of deionised water, and stirred on a magnetic stirrer at room temperature for 15 min. A base solution was prepared in another beaker by adding 4 g of NaOH in 60 ml deionised water. This solution was then poured into the beaker containing the metal precursors. The stirring was continued at room temperature and then thick precipitates was observed immediately after the addition of base solution. The reaction mixture was then exposed to high-intensity ultrasonic irradiation (frequency: 20 kHz and power: 70 W) (Ultrasonic homogenizer UZ SONOPULS HD 2070) for 20 min. After the completion of the sonication for 20 min, the precipitate was centrifuged, and washed with deionised water three-four times and dried in oven at 40 °C. Following above procedures, other samples were prepared for 40 min, 60 min, and 80 min of sonication time. These prepared nanoparticles were named as MF20, MF40, MF60, and MF80 corresponding to sonication time 20 min, 40 min, 60 min, and 80 min, respectively. The above samples were synthesized by using 50% amplitude of the ultrasonic power input. Further, $MnFe_2O_4$ spinel ferrite nanoparticles were synthesized by this sonochemical method at different percentage amplitude of ultrasonic power input. The percentage (%) amplitude of ultrasonic power input was 75% and 100% for a constant time 60 min and these synthesized samples were named as MF-P75 and MF-P100, respectively. During sonochemical synthesis, water decomposes to provide hydrogen and hydroxyl radicals [39]. These created hydrogen radicals may combine to produce hydrogen and also the hydroxyl radicals may combine to provide hydrogen peroxide. Further, iron nitrate and manganese nitrate hydrolyse to provide their corresponding hydroxides [40]. Furthermore, there is formation of oxides by initiation of oxidation of their corresponding hydroxides under ultrasonic cavitation. In addition, all formed oxides Fe_3O_4 and Mn_3O_4 due to ultrasound cavitation oxidizes to form $MnFe_2O_4$ spinel ferrite [41].

2.3. Characterization

The crystal phase formation of $MnFe_2O_4$ nanoparticles at different sonication time was investigated by using Rigaku MiniFlex 600 X-ray Spectrometer. The Raman modes related to vibration of metal ion-oxygen ion at octahedral site and tetrahedral site in $MnFe_2O_4$ at different sonication time were investigated by Raman microscope Nicolet DXR. The absorption band associated to vibration of metal ions at octahedral and tetrahedral sites in $MnFe_2O_4$ nanoparticles at different sonication time were studied by using FTIR spectrometer Nicolet 6700 (Thermo Scientific). The morphology of the particles of $MnFe_2O_4$ spinel ferrite at different sonication time was investigated by the field emission scanning electron microscopy (FE-SEM) and elemental analysis was done by energy dispersive X-ray spectroscopy (EDX) by scanning electron microscope Nova NanoSEM450 (FEI company). In addition, the morphology and lattice fringes of $MnFe_2O_4$ nanoparticles at different sonication time was examined by the high-resolution transmission electron microscope (JEOL JEM 2100). The oxidation state and cation distribution of prepared $MnFe_2O_4$ nanoparticles at different sonication time was studied by X-ray photoelectron spectroscopy (Kratos Analytical Axis Ultra DLD). The magnetic hysteresis curves of

synthesized $MnFe_2O_4$ spinel ferrite nanoparticles were measured by using a vibrating sample magnetometer (VSM 7407, Lake Shore). The dielectric and electrical characteristics of prepared $MnFe_2O_4$ nanoparticles were examined by using a Broadband Dielectric Impedance Analyzer Concept 40 (Novocontrol, Germany). In addition, the complex impedance characteristics of these prepared $MnFe_2O_4$ nanoparticles were studied by a standard sample cell BDS 1200 employing RC model. The specific surface area was calculated based upon the multipoint Brunauer-Emmet-Teller analysis of nitrogen adsorption/desorption isotherms at 77 K recorded by Belsorp-mini II (BEL Japan, Inc.). Samples were outgassed for 3 h at 80 °C prior to the measurements. Optical property was investigated by using diffuse reflectance spectroscopy (Lambda 1050 UV/VIS/NIR spectrometer from Perkin Elmer).

3. Result and discussion

3.1. X-ray diffraction study

X-ray diffraction technique is utilized to investigate the structural formation and evolution of sonochemically prepared $MnFe_2O_4$ nanoparticles with increase of sonication time and percentage amplitude of ultrasonic power input. Fig. 1 depicts the X-ray Diffraction pattern of prepared $MnFe_2O_4$ nanoparticles by sonochemical synthesis method. The prepared $MnFe_2O_4$ nanoparticles exhibited a single phase cubic spinel structure. The observed diffraction peak in prepared $MnFe_2O_4$ nanoparticles can be index to (1 1 1), (2 2 0), (3 1 1), (2 2 2), (4 0 0), (4 2 2), (5 1 1), and (4 4 0) corresponding to plane of cubic unit cell of the cubic spinel structure [42,43]. The observed broadening in the X-ray diffraction peak of prepared $MnFe_2O_4$ nanoparticles at lower sonication time indicate the nanocrystalline nature of the prepared $MnFe_2O_4$ nanoparticles by sonochemical method. The diffraction peak intensity was increased with increase of sonication time and percentage amplitude of ultrasonic power input, which indicate the increase of crystallinity and crystallite size. The observed lower diffraction intensity with broad diffraction peak of amorphous like/nano-crystalline nature of prepared spinel ferrite at low sonication time attribute that there was less nucleus activation energy to form highly crystalline spinel ferrite nanoparticles at lower sonication time [44]. The average crystallite size of prepared $MnFe_2O_4$ spinel ferrite nanoparticles was evaluated by using the Scherrer formula:

$$d = \frac{k\lambda}{\beta cos\theta}$$

where k is 0.9, λ is the X-ray wavelength, β is the full width at half maximum of the (3 1 1) diffraction peak of $MnFe_2O_4$ spinel ferrite nanoparticles, and θ is the diffraction angle. The average crystallite sizes of prepared nanoparticles were noticed to increase from 1.8 nm to 22.1 nm, with increase of sonication time 20 min to 80 min at constant 50% amplitude of ultrasonic power input, as tabulated in Table 1. However, the crystallite size was increased from 19.3 nm to 25.5 nm with increase of percentage of amplitude of ultrasonic power input at constant sonication time 60 min.

Further, the lattice parameter of sonochemically synthesized $MnFe_2O_4$ spinel ferrite nanoparticles can be determined by using following relation:

$$a = \frac{\lambda(h^2 + k^2 + l^2)^{1/2}}{2Sin\theta}$$

The calculated values of lattice parameter for prepared $MnFe_2O_4$ nanoparticles are tabulated in Table 1. It can be noticed that the lattice parameter was increased with increase of sonication time and percentage amplitude of ultrasonic power input. The lattice parameter of sonochemically prepared $MnFe_2O_4$ nanoparticles was observed to increase from 8.2685 Å to 8.4831 Å with increase of sonication time 20 min to 80 min at constant 50% amplitude of ultrasonic power input. However, the lattice parameter was increased from 8.4551 Å to 8.4972 Å with increase of percentage of amplitude of ultrasonic power input at constant sonication time 60 min. The increase in lattice constant with sonication time and percentage amplitude of power input obeys Vegard's law [45]. In spinel ferrite structure, the lattice constant has correlation with microstructure, surface defects, thermal triggered ordering/reordering of cations, valence states and chemical bonds in this crystal structure [46]. In this work, the increase in lattice constant is associated with variation of microstructure, surface defects and ultrasonic activated ordering/reordering of cations in spinel ferrite crystal. R.D. Raland et al. [47] noticed the increase of lattice parameter from 8.422 Å to 8.459 Å with increase of crystallite size from 19 nm to 32 nm of $MnFe_2O_4$ nanoparticles by co-precipitation method. The X-ray density ($\rho_{X\text{-}ray}$) of synthesized $MnFe_2O_4$ spinel ferrite nanoparticles at different sonication time can be determined by utilizing the following relation:

$$\rho_{X-ray} = \frac{ZM}{N_A a^3}$$

where, Z is the number of molecules per unit cell, M is the molecular weight of $MnFe_2O_4$ spinel ferrite, N_A is the Avogadro's number and 'a' is the lattice parameter of $MnFe_2O_4$ spinel ferrite nanoparticles prepared at different sonication time. The evaluated values of X-ray density of the prepared $MnFe_2O_4$ spinel ferrite nanoparticles at different sonication time are tabulated in Table 1. It was noticed that the X-ray density of sonochemically prepared $MnFe_2O_4$ nanoparticles was decreased with increase of sonication time and percentage amplitude of ultrasonic

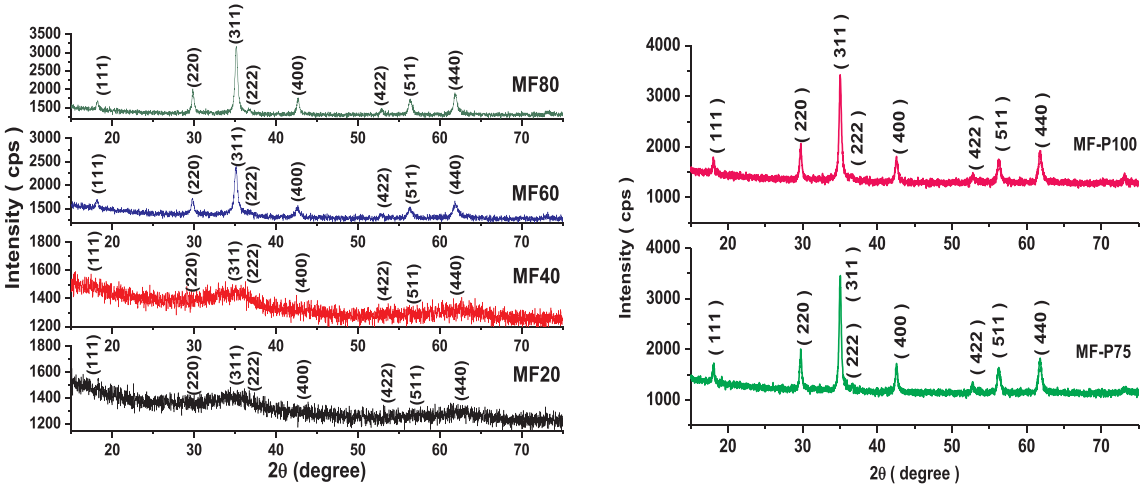

Fig. 1. XRD pattern of $MnFe_2O_4$ spinel ferrite nanoparticles by sonochemical method.

Table 1
Crystallite size, lattice parameter, X-ray density and ionic radii for $MnFe_2O_4$ spinel ferrite nanoparticles synthesized by sonochemical method.

Sample	Sonication time (min)	%Amplitude of Power Input	Crystallite size D (nm)	Lattice Parameter a (Å)	X-ray density dx (g/cm^3)	Ionic Radii	
						r_A (Å)	r_B (Å)
MF20	20	50	1.8	8.2685	5.419	0.5990	0.6727
MF40	40	50	2.0	8.3494	5.263	0.6177	0.6923
MF60	60	50	19.3	8.4551	5.068	0.6423	0.7176
MF80	80	50	22.1	8.4831	5.018	0.6488	0.7144
MF-P75	60	75	22.8	8.4878	5.010	0.6499	0.7255
MF-P100	60	100	25.5	8.4972	4.993	0.6521	0.7278

power input. X-ray density was decreased from 5.419 g/cm^3 to 5.018 g/cm^3 with increase of sonication time from 20 min to 80 min at constant 50% amplitude of ultrasonic power input. However, the X-ray density was decreased from 5.068 g/cm^3 to 4.993 g/cm^3 with increase of percentage of amplitude of ultrasonic power input at constant sonication time 60 min. Kurnia et al. [48] observed the decrease of X-ray density from 5.26 g/cm^3 to 5.04 g/cm^3 with increase of crystallite size 13.1 nm to 18.4 nm for $MnFe_2O_4$ nanoparticles synthesized by co-precipitation method.

Further, the structural parameters such as the tetrahedral and octahedral site radii (r_A and r_B), hopping length in tetrahedral and octahedral site (d_A and d_B), tetrahedral and octahedral bond lengths (d_{Ax} and d_{Bx}), tetrahedral edge, shared and unshared octahedral edges (d_{AxE}, d_{BxE} and d_{BxEU}) for sonochemically prepared $MnFe_2O_4$ nanoparticles can be determined by using following equation [49]:

$$r_A = \left(u - \frac{1}{4}\right)a\sqrt{3} - R_o$$

$$r_B = \left(\frac{5}{8} - u\right)a - R_o$$

$$d_A = \frac{1}{4}a\sqrt{3}$$

$$d_B = \frac{1}{4}a\sqrt{2}$$

$$d_{Ax} = a\sqrt{3}\left(u - \frac{1}{4}\right)$$

$$d_{Bx} = a\left[3u^2 - \left(\frac{11}{4}\right)u + \left(\frac{43}{64}\right)\right]^{1/2}$$

$$d_{AxE} = a\sqrt{2}\left(2u - \frac{1}{2}\right)$$

$$d_{BxE} = a\sqrt{2}\,(1 - 2u)$$

$$d_{BxEU} = a\left[4u^2 - 3u + \left(\frac{11}{16}\right)\right]^{1/2}$$

where, a is the lattice parameter of sonochemically prepared $MnFe_2O_4$ nanoparticles, u is the oxygen positional parameter (u = 0.384 Å), and R_o (=1.32 Å) is the radius of the oxygen. The calculated values of structural parameters for $MnFe_2O_4$ spinel ferrite nanoparticles are tabulated in Tables 1 and 2. The increase of hopping length with increase of sonication time and percentage amplitude of ultrasonic power input was observed. It implies that the distance between the magnetic ions in sonochemically prepared $MnFe_2O_4$ nanoparticles increases with increase of sonication time and percentage of amplitude of ultrasonic power input. It is related with increase of crystallite size and cation redistribution in $MnFe_2O_4$ nanoparticles with increase of sonication time and power. The observed change in structural characteristics triggered by sonication time and power can lead the change in physical characteristics of sonochemically prepared $MnFe_2O_4$ spinel ferrite nanoparticles.

Table 2
Hopping length, tetrahedral bond, octahedral bond, tetrahedral edge, octahedral edge (shared and unshared) for $MnFe_2O_4$ spinel ferrite nanoparticles synthesized by sonochemical method.

Sample	Hopping Length		Tet. Bond d_{Ax} (Å)	Oct. Bond d_{Bx} (Å)	Tet. Edge d_{AxE} (Å)	Oct. Edge (Shared & Unshared)	
	d_A (Å)	d_B (Å)				d_{BxE} (Å)	d_{BxEU} (Å)
MF20	3.5803	2.9229	1.9190	1.9954	3.1334	2.7125	2.9271
MF40	3.6153	2.9515	1.9378	2.0149	3.1640	2.7390	2.9557
MF60	3.6611	2.9888	1.9623	2.0404	3.2041	2.7737	2.9931
MF80	3.6732	2.9987	1.9688	2.0472	3.2147	2.7829	3.0031
MF-P75	3.6752	3.0004	1.9699	2.0483	3.2164	2.7844	3.0047
MF-P100	3.6793	3.0037	1.9721	2.0506	3.2200	2.7874	3.0081

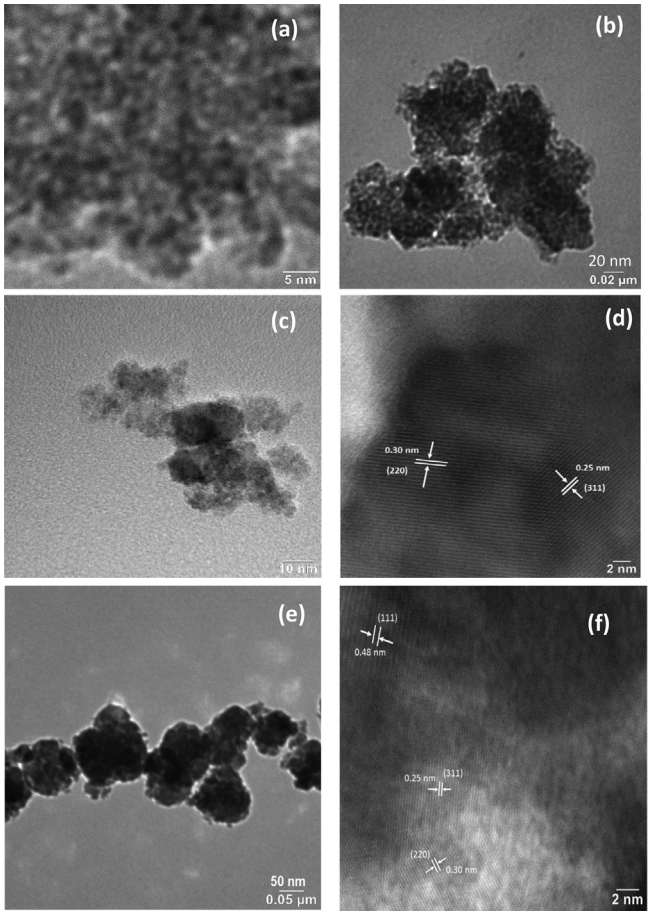

Fig. 2. (a) TEM image of MF20, (b) TEM image of MF40, (c) TEM image of MF60, (d) HRTEM of MF60, (e) TEM image of MF80, and (f) HRTEM of MF80.

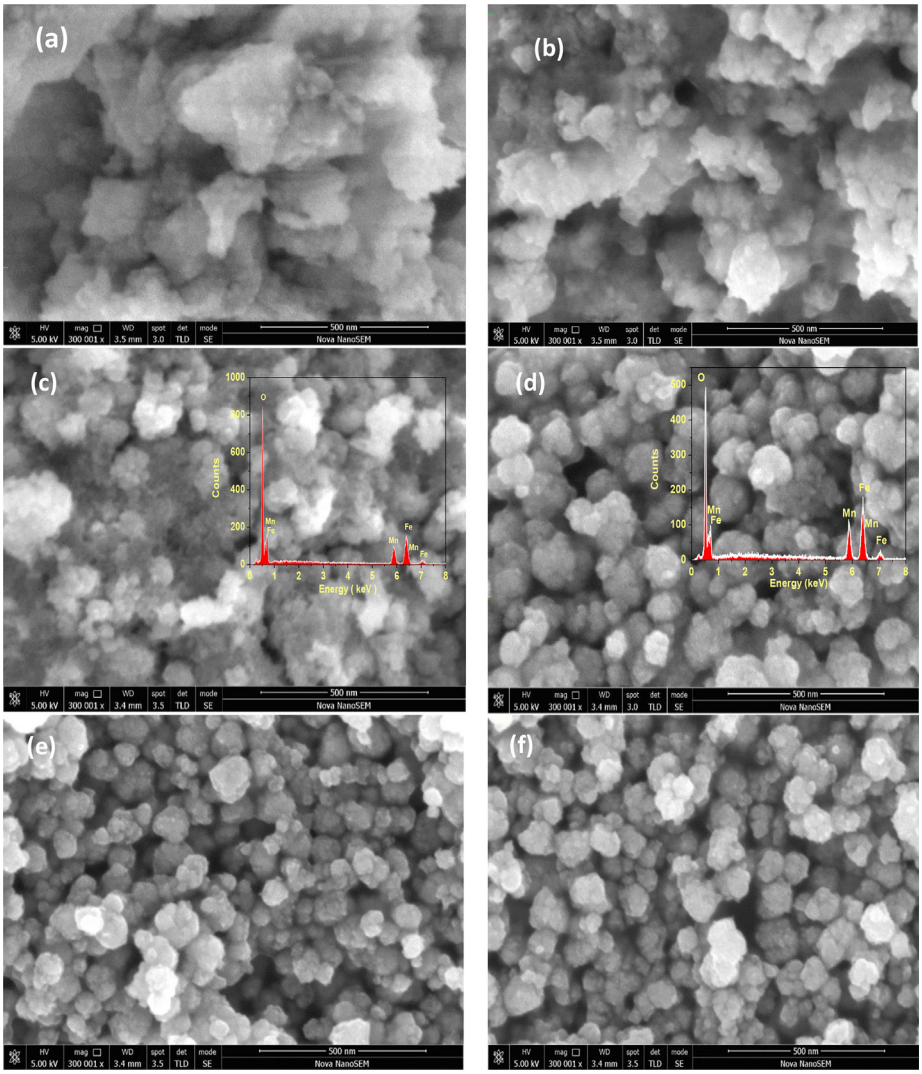

Fig. 3. FE-SEM image of (a) MF20, (b) MF40, (c) MF60, (d) MF80, (e) MF-P75, and (f) MF-P100. EDX spectrum is shown as inset.

3.2. TEM and HRTEM study

Fig. 2 (a & b) shows the TEM image of MF 20 and MF40 sample, which attribute smaller sized spherical nanoparticles of 2–4 nm. Fig. 2(c) depicts TEM image of MF60 sample, which indicate that sample consist of 2–5 nm sized particles with spherical morphology. Fig. 2(d) shows the HRTEM image of MF60 sample, which indicate lattice fringes with inter-planer distance 0.30 nm and 0.25 nm corresponding to plane (2 2 0) and (3 1 1), respectively, for $MnFe_2O_4$ spinel ferrite crystal structure. Fig. 2(e) illustrates the TEM image of MF80 sample, indicating that the sample has spherical nanoparticles of size 50–80 nm, which is also assembly of nanoparticles of 5–10 nm. Fig. 2(f) represents typical HRTEM image of MF80 sample, which is consisted of well resolved two-dimensional lattice fringes with spacing of 0.48 nm, 0.25 nm, and 0.30 nm corresponding to lattice plane (1 1 1), (3 1 1) and (2 2 0), respectively for $MnFe_2O_4$ spinel ferrite system.

3.3. FE-SEM and EDX study

Fig. 3 (a & b) depict the FE-SEM image of MF20 and MF40 samples, which indicates nanocrystalline spinel ferrite of size 2–4 nm. Fig. 3(c) depicts the FE-SEM image of MF60 sample, indicating spherical nanoparticles of 2–5 nm, which is consistent with the TEM image. Further, Fig. 3(d) illustrates the FE-SEM image of MF80 sample, it exhibited spherical nanoparticles of 50–80 nm, which is assembly of nanoparticles of 5–10 nm. Therefore, there was agglomeration of smaller size nanoparticles with increase of sonication time, and further bigger nanoparticles was formed. Fig. 3 (e & f) depict the FE-SEM image of MF-P75 and MF-P100 sample, which indicate increase of size of spherical nanoparticles with increase of the percentage amplitude of ultrasonic power input. The inset in Fig. 3(c-d) is EDX pattern, indicating elemental presence of Mn, Fe and Oxygen in prepared spinel ferrite nanoparticles.

3.4. Raman spectroscopy

Fig. 4 depicts the Raman spectra of sonochemically prepared $MnFe_2O_4$ nanoparticles at different sonication time 20 min, 40 min, 60 min, and 80 min. Theoretical group analysis predicts the five Raman active mode, $A_{1g} + E_g + 3T_{2g}$ for spinel ferrite crystal structure [50]. It can be noticed from Fig. 4 that the Raman spectrum of prepared spinel ferrite nanoparticles exhibited all the characteristics Raman bands, i.e., E_g mode (263 cm^{-1}), T_{2g} mode (216 cm^{-1}, 368 cm^{-1}, 580 cm^{-1}) and A_{1g} mode (610 cm^{-1}, 666 cm^{-1}), which confirm spinel ferrite structure formation of $MnFe_2O_4$ by sonochemical synthesis [51]. In addition, the Raman intensity increases with sonication time, indicating improvement in the crystallinity and crystallite size with increase of sonication time.

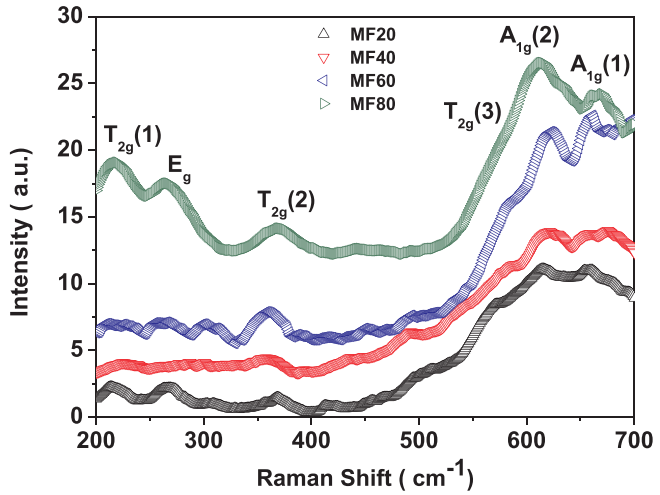

Fig. 4. Raman spectrum of sonochemically synthesized $MnFe_2O_4$ nanoparticles at sonication time 20 min, 40 min, 60 min, and 80 min.

3.5. FTIR spectroscopy

Fig. 5 depicts the FTIR spectra of $MnFe_2O_4$ nanoparticles synthesized at different sonication time 20 min, 40 min, 60 min and 80 min. It can be seen in Fig. 5 that the FTIR spectra consist of two absorption bands, first at high wavenumber side 500–600 cm^{-1} and second at low wavenumber side 200–350 cm^{-1}. The existence of these two absorption bands confirm the spinel ferrite crystal structure formation of $MnFe_2O_4$ nanoparticles by sonochemical synthesis method at different sonication time. The absorption band at high wavenumber side 500–600 cm^{-1} corresponds to intrinsic stretching vibration of metals at tetrahedral sites, however the absorption band at low wavenumber side 200–350 cm^{-1} is associated with octahedral-metal stretching. The observed two absorption band positions in tetrahedral and octahedral complexes of $MnFe_2O_4$ nanoparticles is associated with the different distances between Fe^{3+}–O^{2-} at the octahedral and tetrahedral sites [52]. Further, the shift in vibrational band position is associated with the increase of crystallite size and cation redistribution with increase of sonication time [53].

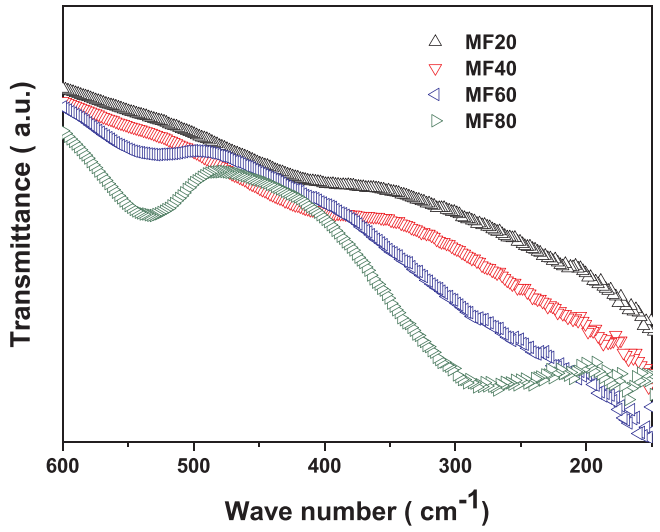

Fig. 5. FTIR spectrum of sonochemically synthesized $MnFe_2O_4$ nanoparticles at sonication time 20 min, 40 min, 60 min, and 80 min.

3.6. X-ray photoelectron spectroscopy

Fig. 6(a) depicts the XPS survey spectrum of MF80 sample, which represent the existence of Fe 2p, Mn 2p and O 1 s peaks at binding energy 710.9 eV, 641.6 eV and 528.5 eV, respectively. The deconvoluted high resolution XPS spectra of Fe 2p for MF20, MF40, MF60, and MF80 sample is shown in Fig. 6(b), (c), (d) & (e), respectively. Fig. 6(b-e) displays the presence of Fe $2p_{3/2}$ and Fe $2p_{1/2}$, with satellite peak for Fe $2p_{3/2}$, confirming the Fe^{3+} oxidation state in $MnFe_2O_4$ nanoparticles synthesized by sonochemical method at different sonication time [54]. Fig. 7 (a-d) illustrates the deconvoluted high resolution XPS spectra of Mn 2p and indicate existence of Mn^{2+} oxidation state in prepared spinel ferrite system [55]. The Fe region as shown in Fig. 6 (b-e) and Mn region as displayed in Fig. 7(a-d) were further fitted and analyzed for cation distribution at octahedral and tetrahedral site in $MnFe_2O_4$ nanoparticles prepared at sonication time 20 min, 40 min, 60 min, and 80 min. Table 3 displays evaluated cation distribution of Fe and Mn at octahedral and tetrahedral site in $MnFe_2O_4$ nanoparticles synthesized by sonochemical synthesis technique at different sonication time 20 min, 40 min, 60 min, and 80 min. It can be noticed that the Fe cation at tetrahedral site was increased, whereas at octahedral site it was decreased with the increase of sonication time. In case of Mn cation, it was altered randomly at octahedral and tetrahedral site. The occupational formula by using X-ray photoelectron spectroscopy for prepared spinel ferrite nanoparticles was $(Mn_{0.29}Fe_{0.42})$ $[Mn_{0.71}Fe_{1.58}]O_4$, $(Mn_{0.34}Fe_{0.48})$ $[Mn_{0.68}Fe_{1.48}]O_4$, $(Mn_{0.32}Fe_{0.52})$ $[Mn_{0.68}Fe_{1.48}]O_4$ and $(Mn_{0.28}Fe_{0.54})$ $[Mn_{0.72}Fe_{1.46}]O_4$ at sonication time 20 min, 40 min, 60 min and 80 min, respectively.

3.7. BET specific area analysis

Fig. 8(a) depicts N_2 adsorption-desorption isotherm curves of synthesized $MnFe_2O_4$ nanoparticles measured at 77 K. The specific surface area of these nanoparticles were evaluated by Brunauer-Emmett-Teller (BET) method [56]. The BET specific surface area were 253.6 m^2/g, 307.4 m^2/g, 162.3 m^2/g, 66.5 m^2/g, and their pore volume were 0.21 cm^3/g, 0.28 cm^3/g, 0.19 cm^3/g and 0.24 cm^3/g for MF20, MF40, MF60 and MF80 sample, respectively. Further, the pore size distribution of these synthesized nanoparticles were evaluated by Barrett-Joyner-Halenda (BJH) method [57], as shown in Fig. 8(b). These porous material is associated with the agglomerates of nanoparticles with approximately uniform spheres. This uniformity of synthesized $MnFe_2O_4$ nanoparticles was decreased at higher sonication time. Furthermore, the average size (d) can be evaluated by using following relation: $d\,(nm) = (6/S_{BET}\rho) * 10^3$, where S_{BET} stands for specific surface area, ρ is the density (4.98 g/cm^3 for $MnFe_2O_4$). The evaluated average particle size by BET specific surface area was 4.75 nm, 3.91 nm, 7.42 nm, and 18.11 nm for MF20, MF40, MF60, and MF80, respectively.

3.8. Magnetic property

Fig. 9 displays the magnetic hysteresis curves of $MnFe_2O_4$ nanoparticles synthesized by sonochemical method. It is noticeable from Fig. 9 that sonochemically synthesized $MnFe_2O_4$ nanoparticles at different sonication time exhibited ferromagnetic characteristics. The saturation magnetization (M_s), remanent magnetization (M_r) and coercivity (H_c) of $MnFe_2O_4$ nanoparticles were evaluated from the magnetic hysteresis curves and mentioned in Table 4. The value of saturation magnetization was increased from 1.9 emu/g to 52.5 emu/g with increase of sonication time 20 min to 80 min at constant 50% amplitude of ultrasonic power input. However, the value of the saturation magnetization was increased from 30.2 emu/g to 59.4 emu/g with increase of the percentage amplitude of ultrasonic power input at constant sonication time 60 min. The increase in saturation magnetization with increase of sonication time and percentage amplitude of ultrasonic

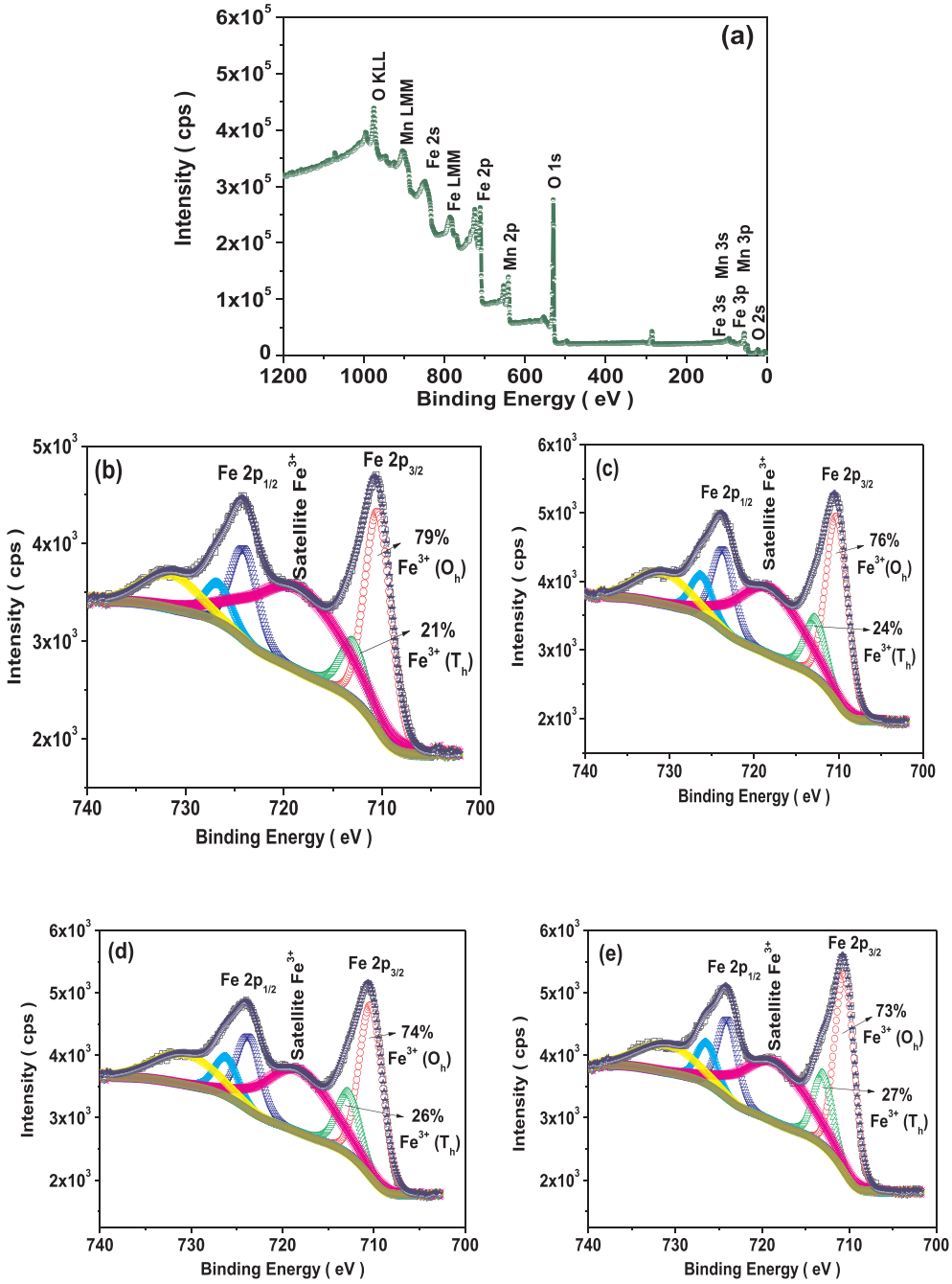

Fig. 6. (a) Survey XPS spectrum of MF80 sample, and high resolution XPS spectrum of Fe 2p of (b) MF20, (c) MF40, (d) MF60, (e) MF80.

power input is associated with the larger particle size and high degree of crystallinity resulting in negligible surface spin canting [58]. The highest value of coercivity (H_c) was observed 45.0 Oe for MF20 sample and it was 24.8 Oe for MF-P100 sample. The coercivity of sonochemically synthesized $MnFe_2O_4$ nanoparticles was decreased with increase of sonication time and percentage amplitude of ultrasonic power input. In general, the coercivity of the spinel ferrite nanoparticles is governed by on the magneto-crystalline anisotropy, strain, inter-particle interaction, grain size, and morphology, etc. [59]. Further, the coercivity is associated with anisotropy constant K by following equation [60]:

$$H_c = \frac{0.96 * K}{M_S}$$

where K is the anisotropy constant and M_s is the saturation magnetization. The evaluated value of anisotropic constant for $MnFe_2O_4$ spinel ferrite nanoparticles is mentioned in Table 4. Furthermore, the magnetic moment (η_B) observed per unit formula in the Bohr Magneton (μ_B) for sonochemically prepared $MnFe_2O_4$ spinel ferrite nanoparticles can be determined by using following relation:

$$\eta_B = \frac{M * M_s}{5585}$$

where M is the molecular weight and M_s is the saturation magnetization of sonochemically prepared $MnFe_2O_4$ nanoparticles. The evaluated value of magnetic moment of prepared $MnFe_2O_4$ nanoparticles is mentioned in Table 4. The highest value of magnetic moment was 2.45 μ_B for MF-P100 sample.

In addition, a comparative property of $MnFe_2O_4$ nanoparticles with same material by other researchers is provided in Table 5, in order to understand the advantage of sonochemical synthesis method.

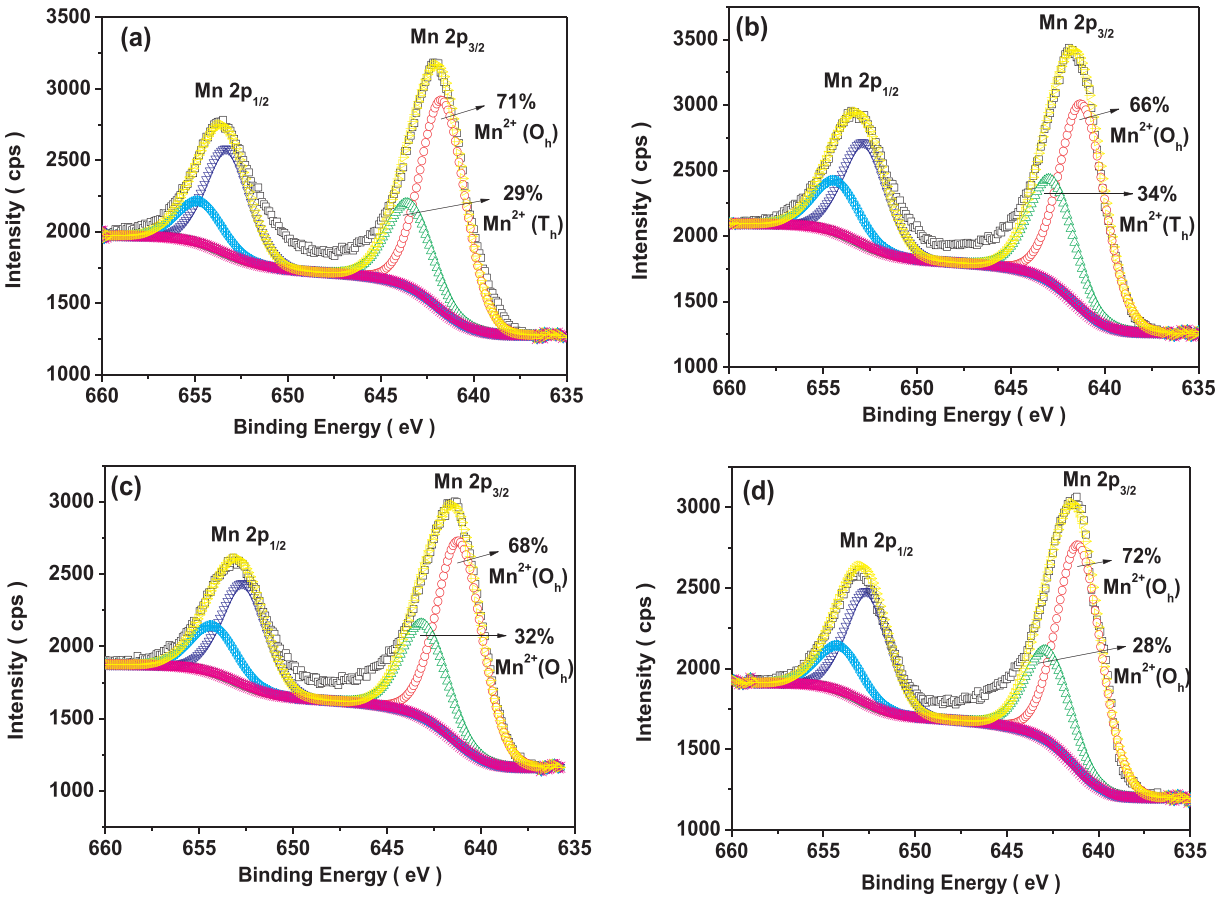

Fig. 7. High resolution XPS spectrum of Mn 2p of (a) MF20, (b) MF40, (c) MF60, (d) MF80.

Table 3
Cation distribution in sonochemically synthesized $MnFe_2O_4$ nanoparticles evaluated by XPS analysis.

Sample	Cation Distribution	
	Tetrahedral (A) site	Octahedral (B) site
MF20	$Mn_{0.29}Fe_{0.42}$	$Mn_{0.71}Fe_{1.58}$
MF40	$Mn_{0.34}Fe_{0.48}$	$Mn_{0.66}Fe_{1.52}$
MF60	$Mn_{0.32}Fe_{0.52}$	$Mn_{0.68}Fe_{1.48}$
MF80	$Mn_{0.28}Fe_{0.54}$	$Mn_{0.72}Fe_{1.46}$

3.9. Optical property

The optical property of prepared $MnFe_2O_4$ spinel ferrite nanoparticles were analysed by diffuse reflectance spectroscopy. The Kubelka-Munk Theory was utilized to evaluate band gap of prepared nanoparticles. The Kubelka-Munk equation can be expressed by the following relation [65]:

$$F(R) = \frac{\alpha}{S} = \frac{(1-R)^2}{2R}$$

where F(R) is the Kubelka-Munk function, α is the absorption coefficient, S is the scattering factor, and R is the reflectance. Kubelka-Munk function is utilized to get equivalent absorption coefficient from the diffuse reflectance. Therefore, the modified Tauc's relation cab be expressed as [66,67]:

$$F(R)h\nu = A(h\nu - E_g)^n$$

where, E_g is the energy gap, A is the proportionality constant, n is the transition coefficient which can be considered as ½ for direct allowed transition. Fig. 10 depicts the modified Tauc's plots $[F(R)E]^2$ versus E (= hν), and the band gap can be evaluated by extrapolating the slop, where $[F(R)\ E]^2 \rightarrow 0$. The determined value of band gap for $MnFe_2O_4$ nanoparticles was found 1.65 eV, 1.62 eV, 1.60 eV and 1.53 eV for MF20, MF40, MF60, MF80 sample, respectively. Several authors reported the band gap analysis by diffuse reflectance spectroscopy. S. Manzoor *et.al.* [68] reported the calculation of band gap of $LaFeO_3$ by Kubelka-Munk function. A. Baykal et al. [69] reported the band gap study by diffuse reflection spectroscopy and noticed the band gap value 1.2 eV – 1.8 eV of Cr^{3+} ion substituted copper ferrite nanoparticles. S. Yuvaraj et al. [70] also studied band gap of $Mn_{0.55}Cu_{0.45}Fe_2O_4$ nanoparticles by diffuse reflection spectroscopy and noticed the band gap variation from 1.46 eV to 1.88 eV at different higher temperature annealing of nanoparticles.

3.10. Dielectric and electrical property

Fig. 11 (a-b) displays the frequency dependent real and imaginary part of dielectric constant of $MnFe_2O_4$ nanoparticles prepared at sonication time 20 min, 40 min, 60 min, and 80 min. It can be observed that the dielectric constant (ε′) of prepared $MnFe_2O_4$ nanoparticles at different sonication time decreases with increase of frequency. It is associated with that at low frequency, the influence of grain boundary is more commanding over that of grains and consequently dielectric dispersion and further at high frequency, the space charge polarization is decreased as the charge carriers are inadequate to follow the applied electric field and results in the decrease of dielectric constant with increase of frequency in prepared $MnFe_2O_4$ nanoparticles at different sonication time [71,72]. Further, the value of dielectric constant was decreased with increase of sonication time. It was decreased from 499 to 8 at 1 kHz frequency for $MnFe_2O_4$ nanoparticles synthesized at

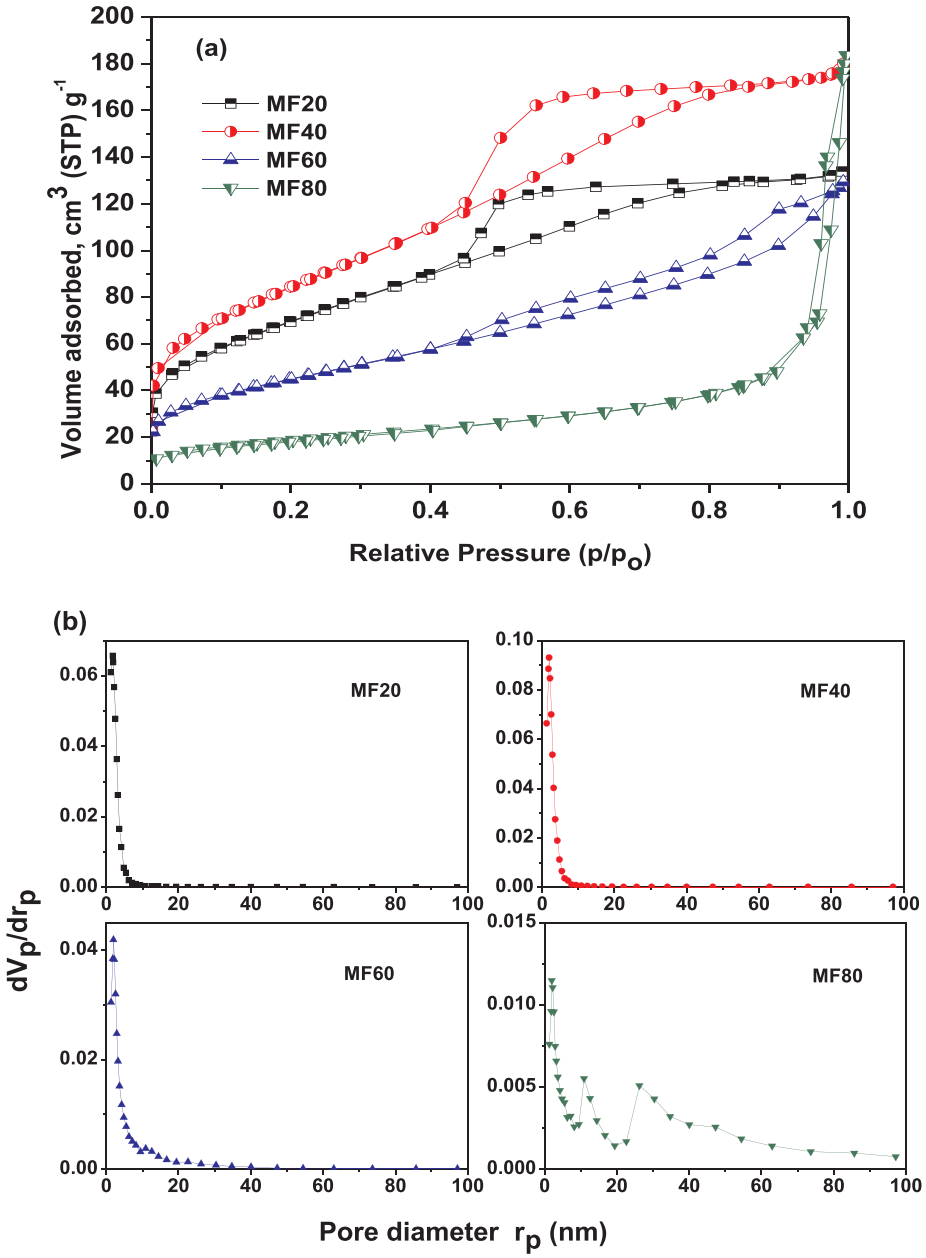

Fig. 8. (a) The N_2 adsorption–desorption isotherms, and (b) pore size distributions of $MnFe_2O_4$ nanoparticles synthesized by sonochemical method.

sonication time from 20 min to 80 min, as mentioned in Table 6. However, it was decreased from 1843 to 16 at 100 Hz for $MnFe_2O_4$ nanoparticles with increase of sonication time 20 min to 80 min. In general, the dielectric constant of $MnFe_2O_4$ spinel ferrite depends on particle size, morphology, cation inversion at octahedral and tetrahedral sites, etc. [73].

Fig. 11(c) depicts the frequency dependent dielectric loss (tanδ) of $MnFe_2O_4$ nanoparticles synthesized at sonication time 20 min, 40 min, 60 min, and 80 min. The observed dielectric loss of $MnFe_2O_4$ nanoparticles at different sonication time decreases with increase of the frequency and further it becomes constant at higher frequency. It is due to the polarization lag behind the applied electric field and it depends on the grain boundaries, impurities and imperfections in the $MnFe_2O_4$ spinel ferrite nanoparticles synthesized at different sonication time [74]. The value of dielectric loss decreases from 2.49 to 0.89 at 1 kHz for $MnFe_2O_4$ nanoparticles with increase of sonication time 60 min to 80 min. In addition, it decreases from 5.92 to 1.67 at 100 Hz from sonication time 60 to 80 min, as mentioned in Table 6.

Further, Fig. 11(d) illustrates the frequency dependent ac conductivity of prepared $MnFe_2O_4$ nanoparticles at sonication time 20 min, 40 min, 60 min, and 80 min. In $MnFe_2O_4$ spinel ferrite nanoparticles, the conduction is due to hopping of electrons between the ions of the same element by the following relation [75]:

$$Mn^{2+} + Fe^{3+} \leftrightarrow Mn^{3+} + Fe^{2+}$$

where Fe^{3+} and Mn^{2+} ions occupy the octahedral sites. The cation distribution at octahedral site can influence the ac conductivity of $MnFe_2O_4$ nanoparticles. From the XPS analysis, it is found that the Fe^{3+} ions at octahedral site decreases with increase of sonication time. Consequently, there is decrease in ac conductivity of prepared $MnFe_2O_4$ nanoparticles with increase of sonication time. The value of ac conductivity decreases from 368×10^{-9} S/cm to 3.1×10^{-9} S/cm at 1 kHz for $MnFe_2O_4$ nanoparticles prepared at sonication time from 20 min to 80 min. In addition, it decreases from 178×10^{-9} S/cm to 1.6×10^{-9} S/cm at 100 Hz for $MnFe_2O_4$ nanoparticles prepared with increase of sonication time from 20 min to 80 min, as mentioned in

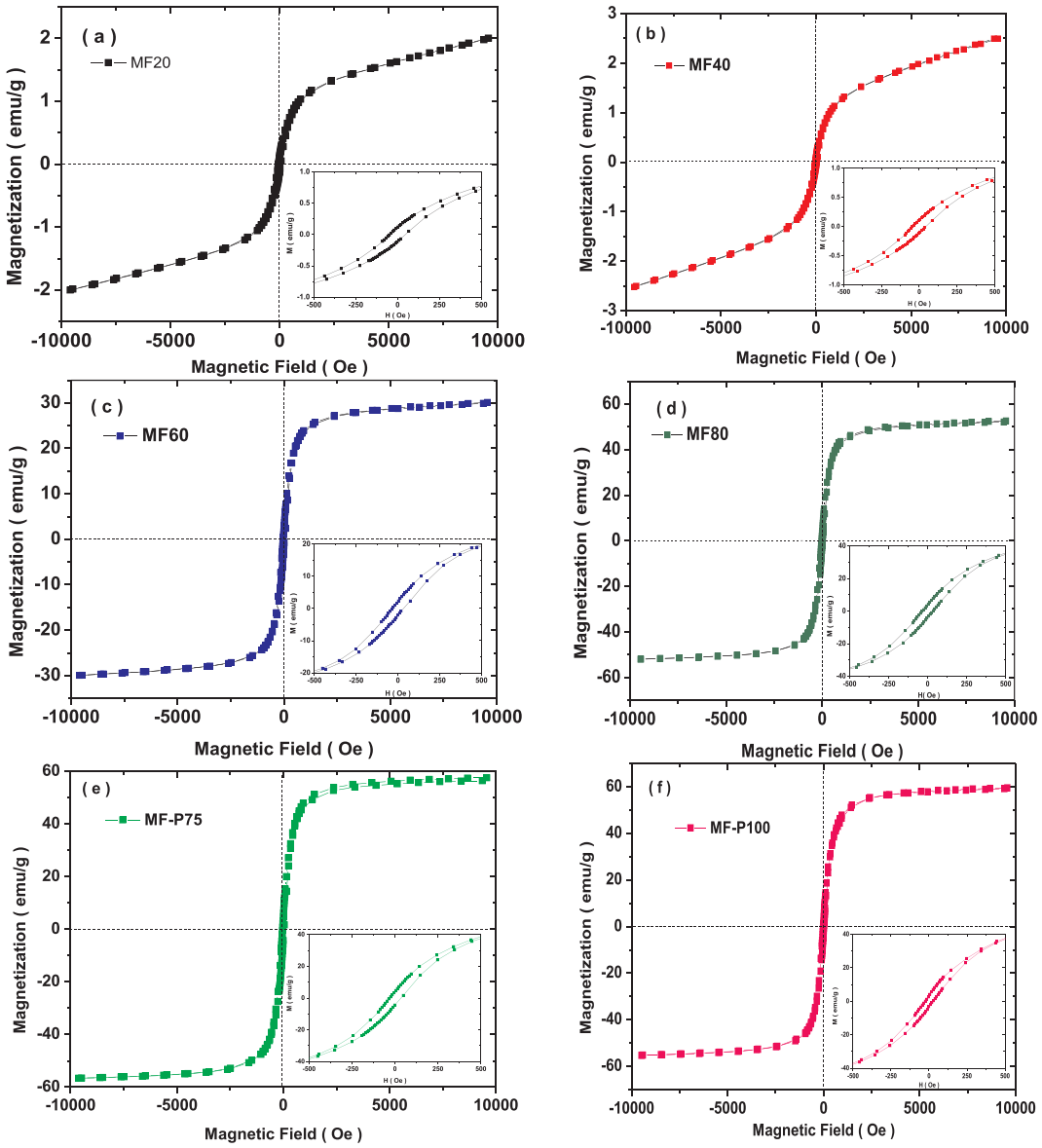

Fig. 9. Magnetic hysteresis curves for $MnFe_2O_4$ nanoparticles synthesized by sonochemical synthesis method.

Table 4
Magnetic parameters for $MnFe_2O_4$ nanoparticles synthesized by sonochemical method.

Sample	Ms (emu/g)	Hc (Oe)	Mr (emu/g)	Mr/Ms	η_B (μ_B)	K ($\times 10^3$ erg./g)
MF20	1.9	45.0	0.12	0.061	0.08	0.09
MF40	2.5	42.0	0.13	0.052	0.10	0.11
MF60	30.2	34.0	2.27	0.075	1.24	1.07
MF80	52.5	32.0	4.50	0.086	2.17	1.75
MF-P75	56.1	33.5	3.99	0.071	2.32	1.95
MF-P100	59.4	24.8	3.41	0.057	2.45	1.53

Table 5
A comparison of $MnFe_2O_4$ nanoparticles prepared by sonochemical synthesis approach and various other approaches by other research groups.

Synthesis Method	Ms (emu/g)	Crystallinity	References
Sonochemical Method	59.4	Highly Crystalline	In this work
Sol-gel combustion method	51.4	Good Crystalline	[61]
Co-precipitation	22.0	Not Well crystalline	[62]
Ball Milling technique	41.0	Good Crystalline	[63]
Hydrothermal Method	41.8	Good Crystalline	[64]

Table 6.

3.11. Impedance and modulus spectroscopy

The prepared $MnFe_2O_4$ spinel ferrite nanoparticles were investigated by the impedance and modulus spectroscopy to correlate the dielectric and electrical characteristics with microstructures. Fig. 12 (a) shows the frequency dependent real part of impedance (Z′) of $MnFe_2O_4$ nanoparticles at sonication time 20 min, 40 min, 60 min and 80 min. The observed decrease in real part of impedance of $MnFe_2O_4$ nanoparticles with increase of frequency, supports the observed increase of ac conductivity with increase of frequency. The decrease in real part of impedance (Z′) with increase of frequency is due to space charge polarization in $MnFe_2O_4$ spinel ferrite nanoparticle [76]. Fig. 12 (b) shows the frequency dependence imaginary part of impedance (Z″) of sonochemically prepared $MnFe_2O_4$ nanoparticles at different sonication time. The imaginary part of impedance (Z″) decreases with increase of frequency for sonochemically prepared $MnFe_2O_4$ nanoparticles. The

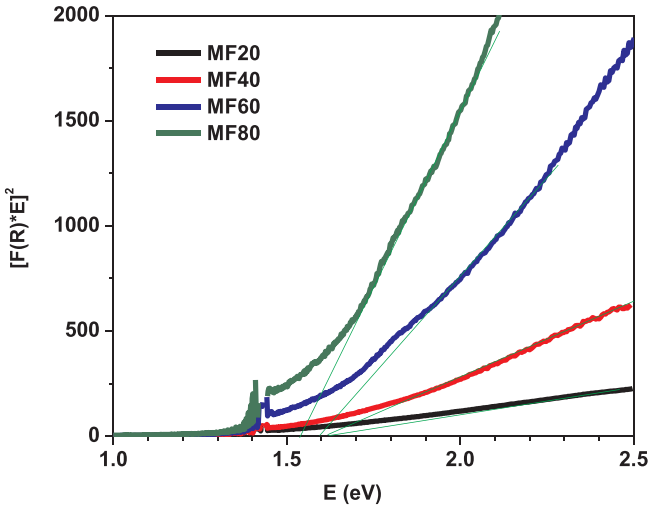

Fig. 10. $[F(R)*E]^2$ vs. E (eV) graph for band gap determination of synthesized $MnFe_2O_4$ nanoparticles by sonochemical method.

decrease in imaginary part of impedance (Z″) of $MnFe_2O_4$ nanoparticles is associated with its inverse relation with frequency [77]. Further, Fig. 12(c) illustrates the frequency dependent real part of modulus (M′) of $MnFe_2O_4$ nanoparticles prepared at different sonication time. The real part of the modulus (M′) of sonochemically prepared $MnFe_2O_4$ nanoparticles increases with increase of frequency and it exhibited two plateau region which specifies with the two different relaxation dynamics. The frequency dependent imaginary part of modulus (M″) of $MnFe_2O_4$ nanoparticles prepared at different sonication time is shown in Fig. 12(d). The peak at lower frequency side in M″ spectra is due to long range hopping of charge carriers from one ionic site to the

Table 6
Dielectric constant (ε′), dielectric loss (tanδ), and ac conductivity (σ) for $MnFe_2O_4$ nanoparticles synthesized at sonication time 20 min, 40 min, 60 min and 80 min.

Sample	ε′		tanδ		σ × 10^{-9} (S/cm)	
	1 kHz	100 Hz	1 kHz	100 Hz	1 kHz	100 Hz
MF20	499	1843	1.37	1.77	368	178
MF40	204	964	1.84	2.33	204	122
MF60	14	47	2.49	5.92	19.5	15.4
MF80	8	16	0.89	1.67	3.1	1.6

neighbouring ionic site at grain boundaries, whereas, the peak at higher frequency side is associated with the short range hopping of charge carriers between ions localized at grains [78]. Furthermore, Fig. 12(e) represents the Cole-cole plots (M′ vs. M″) for $MnFe_2O_4$ nanoparticles prepared at sonication time 20 min, 40 min, 60 min, and 80 min. The $MnFe_2O_4$ nanoparticles synthesized at higher sonication time exhibited well appearance of two semicircles in cole-cole plot. In cole-cole plots of $MnFe_2O_4$ nanoparticles, the observed semicircle, at the higher frequency side is associated with the grain conduction, whereas, it at the lower frequency side is associated with the grain boundary conduction. In addition, the two semicircular peaks provide two type of relaxation phenomenon with different relaxation time (τ) present in $MnFe_2O_4$ nanoparticles prepared at different sonication time. The relaxation time (τ), capacitance (C) and resistance (R) for prepared $MnFe_2O_4$ nanoparticles at different sonication time can be evaluated by using following relation [79]:

$$\tau = \frac{1}{2\pi f_{M''}}$$

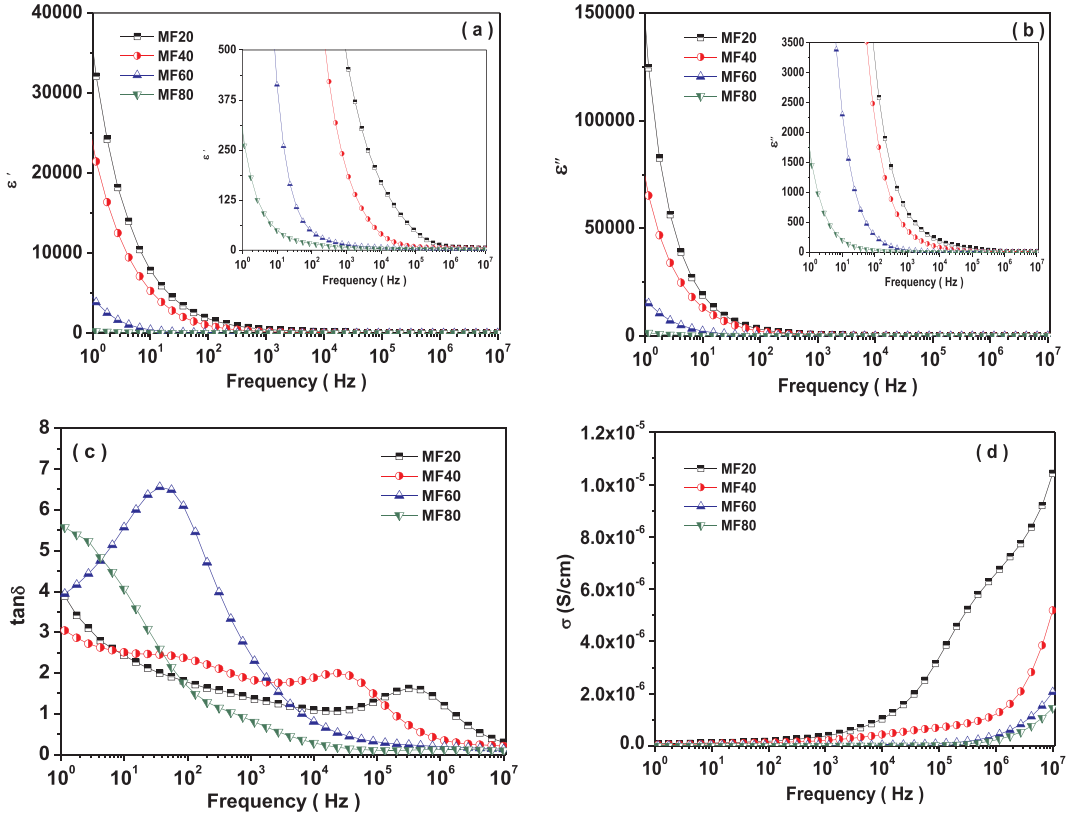

Fig. 11. Frequency dependent (a) real part of dielectric constant (ε′) (Inset is enlarge view) (b) imaginary part of dielectric constant (ε″) (inset is enlarge view), (c) dielectric loss, and (d) ac conductivity of $MnFe_2O_4$ nanoparticles synthesized by sonochemical method at sonication time 20 min, 40 min, 60 min and 80 min.

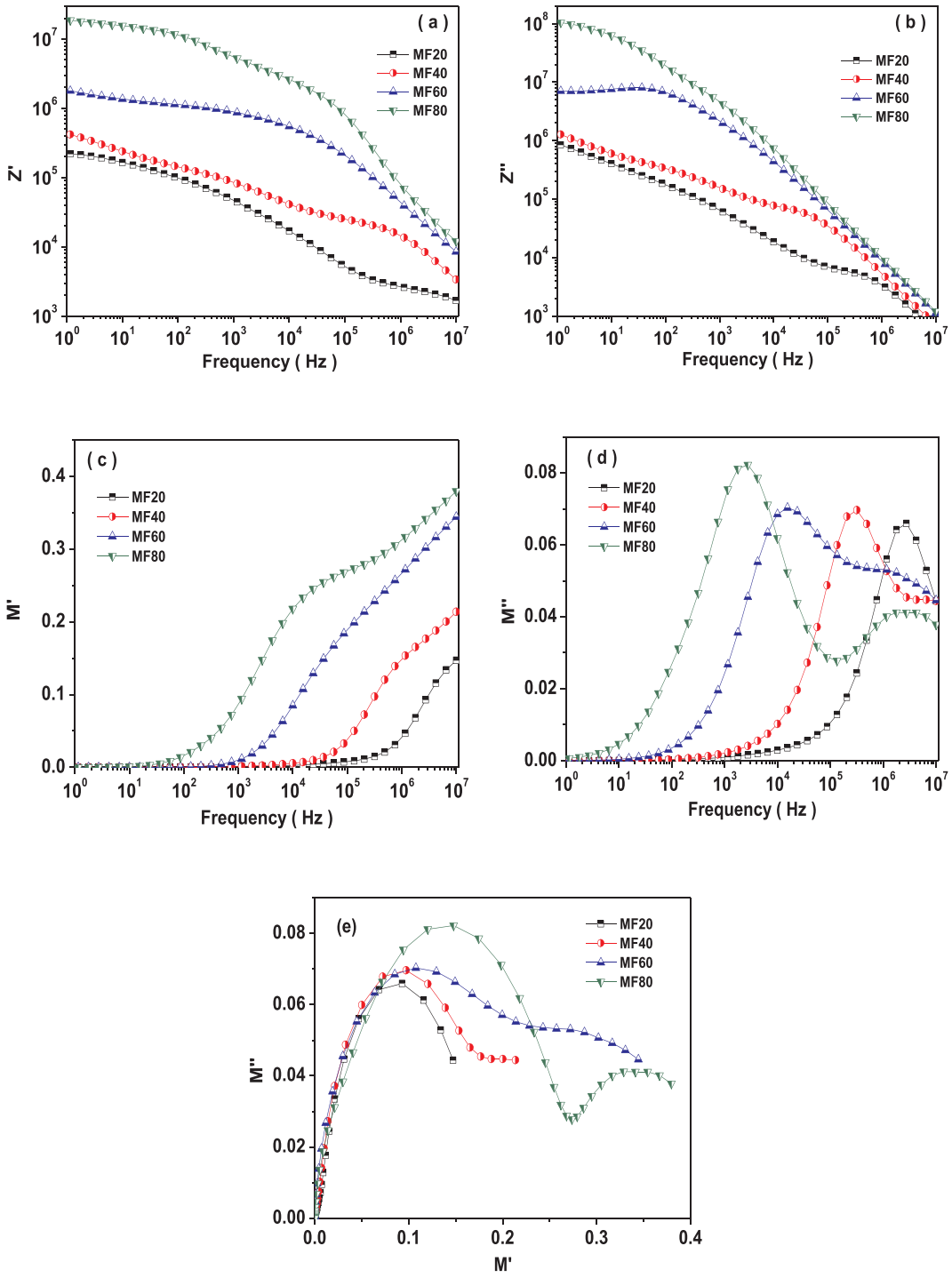

Fig. 12. (a) frequency dependent real part of impedance (Z′), (b) frequency dependent imaginary part of impedance (Z″), (c) frequency dependent real part of modulus (M′), (d) frequency dependent imaginary part of modulus (M″), and (e) cole–cole plots, of $MnFe_2O_4$ nanoparticles synthesized by sonochemical synthesis method at sonication time 20 min, 40 min, 60 min, and 80 min.

$$M'' = \frac{\epsilon_o}{2C}$$

$$2\pi fRC = 1$$

The resistance (R_g, R_{gb},) capacitance (C_g, C_{gb}) and relaxation time (τ_g τ_{gb}) of the grain and grain boundary for $MnFe_2O_4$ spinel ferrite nanoparticles prepared at sonication time 20 min, 40 min, 60 min, and 80 min, are evaluated using above relation and mentioned in Table 7. It was noticed that these evaluated parameters for $MnFe_2O_4$ spinel ferrite nanoparticles were varied with variation of sonication time [80]. The grain boundary relaxation time (τ_{gb}) increases from 0.06 μs to 66.8 μs for $MnFe_2O_4$ nanoparticles prepared at sonication time form 20 min to 80 min. The grain relaxation time (τ_g) decreases from 0.13 μs to 0.05 μs for nanoparticles prepared at sonication time form 60 min to 80 min. Further, the grain boundary resistance (R_{gb}) increases from 0.90 kΩ to 1210 kΩ for sonochemically prepared $MnFe_2O_4$ nanoparticles prepared at sonication time form 20 min to 80 min. The grain resistance (R_g) decreases from 1.49 kΩ to 0.46 kΩ for nanoparticles prepared at sonication time form 60 min to 80 min. Furthermore, the grain boundary capacitance (C_{gb}) decreases from 68.2 pF to 55.4 pF for sonochemically

Table 7
Grain boundary relaxation time (τ_{gb}), grain relaxation time (τ_g), grain boundary resistance (R_{gb}), grain resistance (R_g), grain boundary capacitance (C_{gb}) and grain capacitance (C_g) for $MnFe_2O_4$ nanoparticles at different sonication time 20 min, 40 min, 60 min, and 80 min.

Sample	τ_{gb} (μs)	τ_g (μs)	R_{gb} (kΩ)	R_g (kΩ)	C_{gb} (pF)	C_g (pF)
MF20	0.06	–	0.90	–	68.2	–
MF40	0.51	–	7.95	–	64.2	–
MF60	10.2	0.13	161	1.49	63.3	83.6
MF80	66.8	0.05	1210	0.46	55.4	108.1

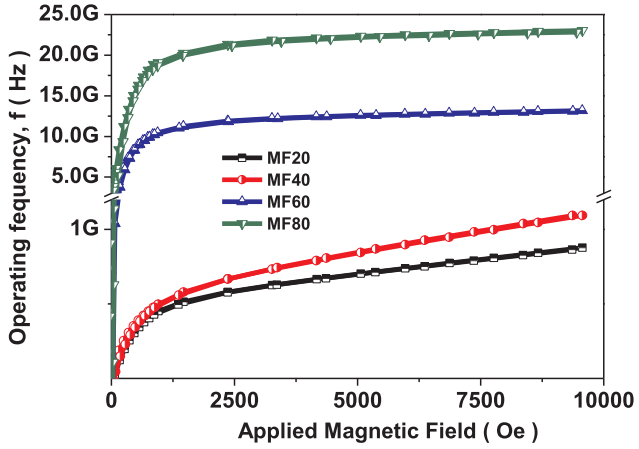

Fig. 13. Optimized operating microwave frequency f ($f = \omega_m/2\pi$) vs. applied magnetic field for synthesized $MnFe_2O_4$ nanoparticles at sonication time 20 min, 40 min, 60 min, and 80 min.

prepared $MnFe_2O_4$ spinel ferrite nanoparticles prepared at sonication time form 20 min to 80 min. However, the grain capacitance (C_g) increases from 83.6 pF to 108.1 pF for spinel ferrite nanoparticles prepared at sonication time form 60 min to 80 min. Similar, variation of these electrical parameters with variation of particle size of $ZnFe_2O_4$ and $NiFe_2O_4$ nanoparticles synthesized by sol–gel combustion method was noticed [81,82].

3.12. Operating microwave frequency study

The investigation of the operating microwave frequency is important for the application of spinel ferrite in devices by industrialist. Fig. 13 depicts the optimized operating microwave frequency of synthesized $MnFe_2O_4$ nanoparticles at sonication time 20 min, 40 min, 60 min, and 80 min. The operating microwave frequency for sonochemically synthesized $MnFe_2O_4$ nanoparticles at different sonication time can be evaluated by using the following relation [83]:

$$\omega_m = 8\pi^2 M_s \cdot \gamma$$

where γ is the gyromagnetic ratio and its value is 2.8 MHz/Oe; Ms is the saturation magnetization. It can be noticed from Fig. 13 that the MF80 sample has optimized operated frequency in the range of 21.6 GHz–23.0 GHz, whereas, MF60 sample has in the range of 12.0 GHz–13.3 GHz. In addition, MF40 and MF20 sample have operated frequency in the range of 0.58–1.10 GHz. The proposed frequency range of these $MnFe_2O_4$ nanoparticles will be fruitful for fabrication of devices at high frequency applications.

4. Conclusion

In summary, $MnFe_2O_4$ nanoparticles were successfully prepared by sonochemical synthesis method at different sonication time and percentage amplitude of ultrasonic power input. XRD study confirms the cubic spinel ferrite structure with absence of any impurity phases. The crystallite size of spinel ferrite nanoparticles was noticed to increase from 1.8 nm to 22.1 nm with increase of sonication time. The lattice parameter of $MnFe_2O_4$ nanoparticles was observed to increase from 8.2685 Å to 8.4831 Å with increase of sonication time 20 min to 80 min. FE-SEM study revealed that $MnFe_2O_4$ nanoparticles prepared at sonication time 60 min exhibited spherical nanoparticles of 2–5 nm, which is consistent with the TEM analysis result, whereas, nanoparticles prepared at sonication time 80 min exhibited spherical nanoparticles of 50–80 nm, which is assembly of nanoparticles of 5–10 nm. Raman spectrum exhibited all the characteristics Raman bands, which confirm spinel ferrite structure formation of $MnFe_2O_4$ by sonochemical synthesis. The increase in the Raman intensity was noticed with increase of the sonication time, which point out the improvement in the crystallinity and crystallite size with increase of sonication time. FTIR study indicate the existence of two absorption bands which approves the spinel ferrite crystal structure formation of $MnFe_2O_4$ spinel ferrite nanoparticles by sonochemical synthesis method at different sonication time. XPS study confirms the cation redistribution in prepared spinel ferrite nanoparticles with increase of sonication time. The occupational formula revealed by XPS study was $(Mn_{0.29}Fe_{0.42})[Mn_{0.71}Fe_{1.58}]O_4$, $(Mn_{0.34}Fe_{0.48})[Mn_{0.68}Fe_{1.48}]O_4$, $(Mn_{0.32}Fe_{0.52})$ $[Mn_{0.68}Fe_{1.48}]O_4$ and $(Mn_{0.28}Fe_{0.54})[Mn_{0.72}Fe_{1.46}]O_4$ for prepared nanoparticles at sonication time 20 min, 40 min, 60 min and 80 min, respectively. The saturation magnetization was increased from 1.9 emu/g to 52.5 emu/g with increase of sonication time 20 min to 80 min at constant 50% amplitude of ultrasonic power input, whereas, it was increased from 30.2 emu/g to 59.4 emu/g with increase of the percentage amplitude of ultrasonic power input at constant sonication time 60 min. Dielectric constant was decreased from 499 to 8 at 1 kHz frequency for $MnFe_2O_4$ spinel ferrite nanoparticles prepared at sonication time from 20 min to 80 min. The value of ac conductivity decreases from 368×10^{-9} S/cm to 3.1×10^{-9} S/cm at 1 kHz for prepared nanoparticles at sonication time from 20 min to 80 min. Electrical parameters such as grain and grain boundary resistance, capacitance and relaxation time was varied for prepared nanoparticles with variation of sonication time. Therefore, the physical characteristics such as magnetic, dielectric, ac conductivity, impedance and modulus spectroscopy characteristics of $MnFe_2O_4$ nanoparticles can be controlled by sonication time for specific application. The evaluated microwave operating frequency suggest that these prepared nanoparticles are potential candidate for their use in fabrication of devices at high microwave frequency applications.

Declaration of Competing Interest

The authors declare that they have no known competing financial interests or personal relationships that could have appeared to influence the work reported in this paper.

Acknowledgement

This work was financially supported by the Czech Science Foundation (GA19-23647S) project at Centre of Polymer Systems, Tomas Bata University in Zlin, Czech Republic.

Appendix A. Supplementary data

Supplementary data to this article can be found online at https://doi.org/10.1016/j.ultsonch.2019.104839.

References

[1] N. Kouki, S. Hcini, M. Boudard, R. Aldawas, A. Dhahrie, Microstructural analysis, magnetic properties, magnetocaloric effect, and critical behaviors of $Ni_{0.6}Cd_{0.2}Cu_{0.2}Fe_2O_4$ ferrites prepared using the sol–gel method under different sintering temperatures, RSC Adv. 9 (2019) 1990.
[2] R. Tanwar, U.K. Mandal, Photocatalytic activity of $Ni_{0.5}Zn_{0.5}Fe_2O_4$@polyaniline

decorated BiOCl for azo dye degradation under visible light–integrated role and degradation kinetics interpretation, RSC Adv. (2019) 8977.
[3] B. Zeynizadeh, S. Rahmani, Sulfonyl-bridged (copper-immobilized nickel ferrite) with activated montmorillonite, [($NiFe_2O_4$@Cu)SO_2(MMT)]: a new class of magnetically separable clay nanocomposite systems towards Hantzsch synthesis of coumarinbased 1,4-dihydropyridines, RSC Adv. 9 (2019) 8002.
[4] M. Hennous, E.V. Ramana, D.M. Tobaldi, B.F.O. Costa, M.A. Valente, J. Labrinchac, M. Karmaoui, Synthesis, structure and magnetic properties of multipod-shaped cobalt ferrite nanocrystals, New J. Chem. 43 (2019) 10259.
[5] X. Zhu, N. Guijarro, Y. Liu, P. Schouwink, R.A. Wells, F.L. Formal, S. Sun, C. Gao, K. Sivula, Spinel Structural Disorder Influences Solar-Water-Splitting Performance of $ZnFe_2O_4$ Nanorod Photoanodes, Adv. Mater. 30 (2018) 1801612.
[6] H.L. Andersen, C. Granados-Miralles, M. Saura-Muzquiz, M. Stingaciu, J. Larsen, F. Søndergaard-Pedersen, J.V. Ahlburg, L. Keller, C. Frandsen, M. Christensen, Enhanced intrinsic saturation magnetization of $Zn_xCo_{1-x}Fe_2O_4$ nanocrystallites with metastable spinel inversion, Mater. Chem. Front. 3 (2019) 668.
[7] P. Dolcet, K. Kirchberg, A. Antonello, C. Suchomski, R. Marschall, S. Diodati, R. Muñoz-Espí, K. Landfester, S. Gross, Exploring wet chemistry approaches to $ZnFe_2O_4$ spinel ferrite nanoparticles with different inversion degrees: a comparative study, Inorg. Chem. Front. 6 (2019) 1527.
[8] B. Nandan, M.C. Bhatnagar, S.C. Kashyap, Cation distribution in nanocrystalline cobalt substituted nickel ferrites: X ray diffraction and Raman spectroscopic investigations, J. Phys. Chem. Solids 129 (2019) 298–306.
[9] M. Fantauzzi, F. Secci, M.S. Angotzi, C. Passiu, C. Cannas, A. Rossi, Nanostructured spinel cobalt ferrites: Fe and Co chemical state, cation distribution and size effects by X-ray photoelectron spectroscopy, RSC Adv. 9 (2019) 19171.
[10] S.K. Gore, S.S. Jadhav, V.V. Jadhav, S.M. Patange, Mu. Naushad, R.S. Mane, K.H. Kim, The structural and magnetic properties of dual phase cobalt ferrite, Sci. Rep. 7 (2017) 2524.
[11] M.M. Baig, M.A. Yousuf, P.O. Agboola, M.A. Khan, I. Shakir, M.F. Warsi, Optimization of different wet chemical routes and phase evolution studies of $MnFe_2O_4$ nanoparticles, Ceram. Int. 45 (2019) 12682–12690.
[12] E.R. Kumar, Ch. Srinivas, M.S. Seehra, M. Deepty, I. Pradeep, A.S. Kamzin, M.V.K. Mehar, N. Krisha Mohan, Particle size dependence of the magnetic, dielectric and gas sensing properties of Co substituted $NiFe_2O_4$ nanoparticles, Sens. Actuators, A 279 (2018) 10–16.
[13] L. Zhang, W. Jiao, The effect of microstructure on the gas properties of $NiFe_2O_4$ sensors: Nanotube and nanoparticle, Sens. Actuators, B 216 (2015) 293–297.
[14] M. Abbas, B.P. Rao, Md.N. Islam, K.W. Kim, S.M. Naga, M. Takahashi, CheolGi Kim, Size-controlled high magnetization $CoFe_2O_4$ nanospheres and nanocubes using rapid one-pot sonochemical technique, Ceram. Int. 40 (2014) 3269–3276.
[15] L.I. Granone, R. Dillert, P. Heitjans, D.W. Bahnemann, Effect of the Degree of Inversion on the Electrical Conductivity of Spinel $ZnFe_2O_4$, ChemistrySelect 4 (2019) 1232–1239.
[16] V.G. Harrisa, V. Šepelák, Mechanochemically processed zinc ferrite nanoparticles: Evolution of structure and impact of induced cation inversion, J. Magn. Magn. Mater. 465 (2018) 603–610.
[17] R. Lamouri, M. Tadout, M. Hamedoun, A. Benyoussef, H. Ez-zahraouy, M. Benaissa, O. Mounkachi, Effect of the cations distribution on the magnetic properties of $SnFe_2O_4$: First-principles study, J. Magn. Magn. Mater. 436 (2017) 6–10.
[18] L.I. Granone, A.C. Ulpe, L. Robben, de S. Klimke, M. Jahns, F. Renz, T.M. Gesing, de T. Bredow, Ralf Dillert, D.W. Bahnemann, Effect of the degree of inversion on optical properties of spinel $ZnFe_2O_4$, Phys. Chem. Chem. Phys. 20 (2018) 28267.
[19] L.I. Granone, K. Nikitin, A. Emeline, R. Dillert, D.W. Bahnemann, Effect of the Degree of Inversion on the Photoelectrochemical Activity of Spinel $ZnFe_2O_4$, Catalysts 9 (2019) 434.
[20] J. Kurian, M. Jacob Mathew, Structural optical and magnetic studies of $CuFe_2O_4$, $MgFe_2O_4$ and $ZnFe_2O_4$ nanoparticles prepared by hydrothermal/solvothermal method, J. Magn. Magn. Mater. 451 (2018) 121–130.
[21] R.S. Yadav, J. Havlica, M. Hnatko, P. Šajgalík, C. Alexander, M. Palou, E. Bartoníčková, M. Boháč, F. Frajkorová, J. Masilko, M. Zmrzlý, L. Kalina, M. Hajdúchová, V. Enev, Magnetic properties of $Co_{1-x}Zn_xFe_2O_4$ spinel ferrite nanoparticles synthesized by starch-assisted sol–gel autocombustion method and its ball milling, J. Magn. Magn. Mater. 378 (2015) 190–199.
[22] S.I. El-Dek, Ma.ha.A. Ali, Sara M. El-Zanaty, Shehab E. Ahmed, Comparative investigations on ferrite nanocomposites for magnetic hyperthermia applications, J. Magn. Magn. Mater. 458 (2018) 147–155.
[23] J.H. Bang, K.S. Suslick, Applications of Ultrasound to the Synthesis of Nanostructured Materials, Adv. Mater. 22 (2010) 1039–1059.
[24] M.A. Almessiere, Y. Slimani, S. Guner, M. Sertkol, A. Demir Korkmaz, Sagar E. Shirsath, A. Baykal, Sonochemical synthesis and physical properties of $Co_{0.3}Ni_{0.5}Mn_{0.2}Eu_xFe_{2-x}O_4$ nano-spinel ferrites, Ultrason. – Sonochem. 58 (2019) 104654.
[25] K. Wu, D. Liu, W. Lu, K. Zhang, One-pot sonochemical synthesis of magnetite@reduced graphene oxide nanocomposite for high performance Li ion storage, Ultrason. – Sonochem. 45 (2018) 167–172.
[26] C.U. Okoli, K.A. Kuttiyiel, J. Cole, J. McCutchen, H. Tawfik, R.R. Adzic, D. Mahajan, Solvent effect in sonochemical synthesis of metal-alloy nanoparticles for use as electrocatalysts, Ultrason. – Sonochem. 41 (2018) 427–434.
[27] S. Yuvaraj, R. Kalai Selvan, Vijay Bhooshan Kumar, Ilana Perelshtein, A. Gedanken, S. Isakkimuthu, S. Arumugam, Sonochemical synthesis, structural, magnetic and grain size dependent electrical properties of NdVO4 nanoparticles, Ultrason. Sonochem. 21 (2014) 599–605.
[28] X. Wu, G. Xu, J.-J. Zhu, Sonochemical synthesis of Fe_3O_4/carbon nanotubes using low frequency ultrasonic devices and their performance for heterogeneous sono-persulfate process on inactivation of Microcystis aeruginosa, Ultrason. – Sonochem. 58 (2019) 104634.
[29] R. Sakthivel, S. Kubendhiran, S.-M. Chen, Facile one-pot sonochemical synthesis of Ni doped bismuth sulphide for the electrochemical determination of promethazine hydrochloride, Ultrason. – Sonochem. 54 (2019) 68–78.
[30] A. Gupta, R. Srivastava, Mini submersible pump assisted sonochemical reactors: Large-scale synthesis of zinc oxide nanoparticles and nanoleaves for antibacterial and anti-counterfeiting applications, Ultrason. – Sonochem. 52 (2019) 414–427.
[31] M. Esmaeili-Zare, M. Salavati-Niasari, A. Sobhani, Simple sonochemical synthesis and characterization of HgSe nanoparticles, Ultrason. Sonochem. 19 (2012) 1079–1086.
[32] H. Zheng, M.S. Matseke, T.S. Munonde, The unique Pd@Pt/C core-shell nanoparticles as methanol-tolerant catalysts using sonochemical synthesis, Ultrason. – Sonochem. 57 (2019) 166–171.
[33] R.S. Yadav, I. Kuřitka, J. Vilcakova, J. Havlica, L. Kalina, P. Urbánek, M. Machovsky, D. Skoda, M. Masař, M. Holek, Sonochemical synthesis of Gd^{3+} doped $CoFe_2O_4$ spinel ferrite nanoparticles and its physical properties, Ultrason. – Sonochem. 40 (2018) 773–783.
[34] P. Balasubramanian, R. Settu, S.-M. Chen, T.-W. Chen, G. Sharmila, A new electrochemical sensor for highly sensitive and selective detection of nitrite in food samples based on sonochemical synthesized Calcium Ferrite ($CaFe_2O_4$) clusters modified screen printed carbon electrode, J. Colloid Interface Sci. 524 (2018) 417–426.
[35] N. Lenin, K. Sakthipandi, R. Rajesh Kanna, J. Rajesh, Effect of neodymium ion on the structural, electrical and magnetic properties of nanocrystalline nickel ferrites, Ceram. Int. 44 (2018) 11562–11569.
[36] S.R. Yousefi, O. Amiri, M. Salavati-Niasari, Control sonochemical parameter to prepare pure $Zn_{0.35}Fe_{2.65}O_4$ nanostructures and study their photocatalytic activity, Ultrason. – Sonochem. 58 (2019) 104619.
[37] M.A. Almessiere, Y. Slimani, A.D. Korkmaz, N. Taskhandi, M. Sertkol, A. Baykal, Sagar E. Shirsath, İ. Ercan, B. Ozçelik, Sonochemical synthesis of Eu^{3+} substituted $CoFe_2O_4$ nanoparticles and their structural, optical and magnetic properties, Ultrason. – Sonochem. 58 (2019) 104621.
[38] M.A. Almessiere, Y. Slimani, A.D. Korkmaz, S. Gunere, M. Sertkol, Sagar E. Shirsath, A. Baykal, Structural optical and magnetic properties of Tm^{3+} substituted cobalt spinel ferrites synthesized via sonochemical approach, Ultrason. – Sonochem. 54 (2019) 1–10.
[39] B.R. Reddy, T. Sivasankar, M. Sivakumar, V.S. Moholkar, Physical facets of ultrasonic cavitational synthesis of zinc ferrite particles, Ultrason. Sonochem. 17 (2010) 416–426.
[40] M. Sivakumar, A. Towata, K. Yasui, T. Tuziuti, Y. Iida, A new ultrasonic cavitation approach for the synthesis of zinc ferrite nanocrystals, Curr. Appl. Phys. 6 (2006) 591–593.
[41] M. Sivakumar, A. Towata, K. Yasui, T. Tuziuti, T. Kozuka, Y. Iida, M.M. Maiorov, E. Blums, D. Bhattacharya, N. Sivakumar, M. Ashok, Ultrasonic cavitation induced water in vegetable oil emulsion droplets – a simple and easy technique to synthesize manganese zinc ferrite nanocrystals with improved magnetization, Ultrason. Sonochem. 19 (2012) 652–658.
[42] P.P. Goswami, H.A. Choudhury, S. Chakma, V.S. Moholkar, Sonochemical Synthesis and Characterization of Manganese Ferrite Nanoparticles, Ind. Eng. Chem. Res. 52 (2013) 17848–17855.
[43] G. Wang, D. Zhao, Y. Ma, Z. Zhang, H. Che, J. Mu, X. Zhang, Z. Zhang, Synthesis and characterization of polymer-coated manganese ferrite nanoparticles as controlled drug delivery, Appl. Surf. Sci. 428 (2018) 258–263.
[44] S.-K. Tong, P.-W. Chi, S.-H. Kung, D.-H. Wei, Tuning bandgap and surface wettability of $NiFe_2O_4$ driven by phase transition, Sci. Rep. 8 (2018) 1338.
[45] R.S. Yadav, I. Kuřitka, J. Vilcakova, J. Havlica, J. Masilko, L. Kalina, J. Tkacz, J. Švec, V. Enev, M. Hajdúchová, Impact of grain size and structural changes on magnetic, dielectric, electrical, impedance and modulus spectroscopic characteristics of $CoFe_2O_4$ nanoparticles synthesized by honey mediated sol-gel combustion method, Adv. Nat. Sci.: Nanosci. Nanotechnol. 8 (2017) 14 045002.
[46] R.S. Yadav, J. Havlica, J. Masilko, L. Kalina, J. Wasserbauer, M. Hajdúchová, V. Enev, I. Kuřitka, Z. Kožáková, Effects of annealing temperature variation on the evolution of structural and magnetic properties of $NiFe_2O_4$ nanoparticles synthesized by starch-assisted sol-gel auto-combustion method, J. Magn. Magn. Mater. 394 (2015) 439–447.
[47] R.D. Raland, D. Saikia, C. Borgohain, J.P. Borah, Heating efficiency and correlation between the structural and magnetic properties of oleic acid coated $MnFe_2O_4$ nanoparticles for magnetic hyperthermia application, J. Phys. D: Appl. Phys. 50 (2017) 325004.
[48] Heriansyah Kurnia, E. Suharyadi, Study on The Influence of Crystal Structure and Grain Size on Dielectric Properties of Manganese Ferrite ($MnFe_2O_4$) Nanoparticles, IOP Conf. Series Materials Science and Engineering 202 (2017) 012046.
[49] M.A. Yousuf, M.M. Baig, N.F. Al-Khalli, M.A. Khan, M.F. Aly Aboud, I. Shakir, M.F. Warsi, The impact of yttrium cations (Y^{3+}) on structural, spectral and dielectric properties of spinel manganese ferrite nanoparticles, Ceram. Int. 45 (2019) 10936–10942.
[50] A. Ahlawat, V.G. Sathe, V.R. Reddy, A. Gupta Mossbauer, Raman and X-ray diffraction studies of superparamagnetic $NiFe_2O_4$ nanoparticles prepared by sol–gel auto-combustion method, J. Magn. Magn. Mater. 323 (2011) 2049–2054.
[51] D. Varshney, K. Verma, A. Kumar, Structural and vibrational properties of $Zn_xMn_{1-x}Fe_2O_4$(x = 0.0, 0.25, 0.50, 0.75, 1.0) mixed ferrites, Mater. Chem. Phys. 131 (2011) 413–419.
[52] A. Thakur, P. Kumar, P. Thakur, K. Rana, A. Chevalier, J.-L. Mattei, P. Queffélec, Enhancement of magnetic properties of $Ni_{0.5}Zn_{0.5}Fe_2O_4$ nanoparticles prepared by the co-precipitation method, Ceram. Int. 42 (2016) 10664–10670.
[53] V.J. Angadi, L. Choudhury, K. Sadhana, Hsiang-Lin Liu, R. Sandhya,

S. Matteppanavar, B. Rudraswamy, V. Pattar, R.V. Anavekar, K. Praveena, Structural electrical and magnetic properties of Sc^{3+} doped Mn-Zn ferrite nanoparticles, J. Magn. Magn. Mater. 424 (2017) 1–11.
[54] G. Fan, J. Tong, F. Li, Visible-Light-Induced Photocatalyst Based on Cobalt-Doped Zinc Ferrite Nanocrystals, Ind. Eng. Chem. Res. 51 (2012) 13639–13647.
[55] R.K. Srivastava, P. Xavier, S.N. Gupta, G.P. Kar, S. Bose, A.K. Sood, Excellent Electromagnetic Interference Shielding by Graphene- $MnFe_2O_4$-Multiwalled Carbon Nanotube Hybrids at Very Low Weight Percentage in Polymer Matrix, ChemistrySelect 1 (2016) 5995–6003.
[56] B.Y. Yu, S.-Y. Kwak, Self-assembled mesoporous Co and Ni-ferrite spherical clusters consisting of spinel nanocrystals prepared using a template-free approach, Dalton Trans. 40 (2011) 9989.
[57] P. Bazant, T. Sedlacek, I. Kuritka, D. Podlipny, P. Holcapkova, Synthesis and Effect of Hierarchically Structured Ag-ZnO Hybrid on the Surface Antibacterial Activity of a Propylene-Based Elastomer Blends, Materials 11 (2018) 363.
[58] A.G. Roca, D. Niznansky, J. Poltierova-Vejpravova, B. Bittova, M.A. González-Fernández, C.J. Serna, M.P. Morales, Magnetite nanoparticles with no surface spin canting, J. Appl. Phys. 105 (2009) 114309.
[59] F. Saffari, P. Kamelin, M. Rahimi, H. Ahmadvand, H. Salamati, Effects of Co-substitution on the structural and magnetic properties of $NiCo_xFe_{2-x}O_4$ ferrite nanoparticles, Ceram. Int. 41 (2015) 7352–7358.
[60] B.G. Manju, P. Raji, Synthesis and magnetic properties of nano-sized $Cu_{0.5}Ni_{0.5}Fe_2O_4$ via citrate and aloe vera: A comparative study, Ceram. Int. 44 (2018) 7329–7333.
[61] S.V. Bhandare, R. Kumar, A.V. Anupama, H.K. Choudhary, V.M. Jali, B. Sahoo, Annealing temperature dependent structural and magnetic properties of $MnFe_2O_4$ nanoparticles grown by sol-gel auto-combustion method, J. Magn. Magn. Mater. 433 (2017) 29–34.
[62] R.D. Ralandinliu Kahmei, J.P. Borah, Clustering of $MnFe_2O_4$ nanoparticles and the effect of field intensity in the generation of heat for hyperthermia application, Nanotechnology 30 (2019) 035706.
[63] A. Ceylan, S. Ozcan, Effects of disordered surface structure on the magnetic properties of nanocrystalline $MnFe_2O_4$, Ceram. Int. 41 (2015) 3875–3878.
[64] L.A. Kafshgari, M. Ghorbani, A. Azizi, Synthesis and characterization of manganese ferrite nanostructure by co-precipitation, sol-gel, and hydrothermal methods, Part. Sci. Technol. (2018) 1–7, https://doi.org/10.1080/02726351.2018.1461154.
[65] T.R. Tatarchuk, N.D. Paliychuk, M. Bououdina, B. Al-Najar, M. Pacia, W. Macyk, A. Shyichuk, Effect of cobalt substitution on structural, elastic, magnetic and optical properties of zinc ferrite nanoparticles, J. Alloy. Compd. 731 (2018) 1256–1266.
[66] S. Debnath, R. Das, Study of the optical properties of Zn doped Mn spinel ferrite nanocrystals shows multiple emission peaks in the visible range a promising soft ferrite nanomaterial for deep blue LED, J. Mol. Struct. 1199 (2020) 127044.
[67] R. Monsef, M. Ghiyasiyan-Arani, M. Salavati-Niasari, Application of ultrasound-aided method for the synthesis of $NdVO_4$ nanophotocatalyst and investigation of eliminate dye in contaminant water, Ultrason. – Sonochem. 42 (2018) 201–211.
[68] S. Manzoor, S. Husain, Influence of Zn doping on structural, optical and dielectric properties of $LaFeO_3$, Mater. Res. Express 5 (2018) 055009.
[69] A. Baykal, S. Guner, H. Gungunes, K.M. Batoo, Md. Amir, A. Manikandan, Magneto Optical Properties and Hyperfine Interactions of Cr^{3+} Ion Substituted Copper Ferrite Nanoparticles, J. Inorg. Organomet. Polym Mater. 28 (2018) 2533–2544.
[70] S. Yuvaraj, N. Manikandan, G. Vinitha, Investigation on the behavioral difference in third order nonlinearity and optical limiting of $Mn_{0.55}Cu_{0.45}Fe_2O_4$ nanoparticles annealed at different temperatures, Mater. Res. Express 4 (2017) 115027.
[71] C.G. Koops, On the Dispersion of Resistivity and Dielectric Constant of Some Semiconductors at Audiofrequencies, Phys. Rev. 83 (1951) 121.
[72] L. Chauhan, A.K. Shukla, K. Sreenivas, Dielectric and magnetic properties of Nickel ferrite ceramics using crystalline powders derived from DL alanine fuel in sol–gel auto-combustion, Ceram. Int. 41 (2015) 8341–8351.
[73] N. Ponpandian, P. Balaya, A. Narayanasamy, Electrical conductivity and dielectric behaviour of nanocrystalline $NiFe_2O_4$ spinel, J. Phys.: Condens. Matter 14 (2002) 3221–3237.
[74] R.V. Mangalaraja, P. Manohar, F.D. Gnanam, M. Awano, Electrical and magnetic properties of $Ni_{0.8}Zn_{0.2}Fe_2O_4$/silica composite prepared by sol-gel method, J. Mater. Sci. 39 (2004) 2037–2042.
[75] C. Behera, R.N.P. Choudhary, Piyush R. Das, Size dependent electrical and magnetic properties of mechanically-activated $MnFe_2O_4$ nanoferrite, Ceram. Int. 41 (2015) 13042–13054.
[76] Z.K. Heiba, M.B. Mohamed, M.A. Ahmed, M.A.A. Moussa, H.H. Hamdeh, Cation distribution and dielectric properties of nanocrystalline gallium substituted nickel ferrite, J. Alloy. Compd. 586 (2014) 773–781.
[77] A. Shukla, N. Kumar, C. Behera, R.N.P. Choudhary, Structural and electrical characteristics of (Co, Ti) modified $BiFeO_3$, J. Mater. Sci.: Mater. Electron. 27 (2016) 7115–7123.
[78] M.A. Ali, M.M. Uddin, M.N.I. Khan, F.-U.-Z. Chowdhury, S.M. Haque, Structural, morphological and electrical properties of Sn-substituted Ni-Zn ferrites synthesized by double sintering technique, J. Magn. Magn. Mater. 424 (2017) 148–154.
[79] Z. Wang, M.S. Seehra, Ising-like chain magnetism, Arrhenius magnetic relaxation, and case against 3D magnetic ordering in β-manganese phthalocyanine ($C_{32}H_{16}MnN_8$), J. Phys.: Condens. Matter 28 (2016) 136002.
[80] K. Rasool, M.A. Rafiq, M. Ahmad, Z. Imran, M.M. Hasan, TiO_2 nanoparticles and silicon nanowires hybrid device: Role of interface on electrical, dielectric, and photodetection properties, Appl. Phys. Lett. 101 (2012) 253104.
[81] R.S. Yadav, I. Kuritka, J. Vilcakova, P. Urbanek, M. Machovsky, M. Masar, M. Holek, Structural, magnetic, optical, dielectric, electrical and modulus spectroscopic characteristics of $ZnFe_2O_4$ spinel ferrite nanoparticles synthesized via honey-mediated sol-gel combustion method, J. Phys. Chem. Solids 110 (2017) 87–99.
[82] R.S. Yadav, I. Kuřitka, J. Vilcakova, J. Havlica, J. Masilko, L. Kalina, J. Tkacz, V. Enev, M. Hajdúchová, Structural, magnetic, dielectric, and electrical properties of $NiFe_2O_4$ spinel ferrite nanoparticles prepared by honey-mediated sol-gel combustion, J. Phys. Chem. Solids 107 (2017) 150–161.
[83] M.N. Akhtara, M. Saleem, M.A. Khan, Al doped spinel and garnet nanostructured ferrites for microwave frequency C and X- band applications, J. Phys. Chem. Solids 123 (2018) 260–265.